OXFORD

Conditions and Dynamics of Magma Storage in the Snæfellsnes Volcanic Zone, Western Iceland: Insights from the Búðahraun and Berserkjahraun Eruptions

Maren Kahl [1]*, Enikő Bali[2,3], Guðmundur H. Guðfinnsson[2], David A. Neave [4], Teresa Ubide [5], Quinten H. A. van der Meer[2] and Simon Matthews[2,6]

[1]Institut Für Geowissenschaften, Universität Heidelberg, Im Neuenheimer Feld 234-236, 69120 Heidelberg, Germany; [2]Nordic Volcanological Center, Institute Of Earth Sciences, University Of Iceland, Sturlugata 7, Reykjavík 101, Iceland; [3]Faculty Of Earth Sciences, University Of Iceland, Sturlugata 7, Reykjavík 101, Iceland; [4]Department Of Earth And Environmental Sciences, The University Of Manchester, Oxford Road, Manchester M13 9PL, UK; [5]School Of Earth & Environmental Sciences, The University Of Queensland, St Lucia Campus, Brisbane, Queensland 4072, Australia; [6]Department Of Earth Sciences, University Of Cambridge, Downing Street, Cambridge, CB2 3EQ, UK

*Corresponding author. Telephone: +49 6221 546021. Fax: +49 6221 54 5503. E-mail: Maren.Kahl@geow.uni-heidelberg.de

ABSTRACT

Establishing the conditions and dynamics of pre-eruptive magma storage and transfer within transient transcrustal storage networks is a major focus of quantitative volcanic petrology. In Iceland, the behaviour, conditions and timescales of magmatic processes within on-rift plumbing systems are increasingly well constrained. However, relatively little is known about magma storage and transfer in off-rift zones, despite off-rift volcanoes being able to generate hazardous explosive eruptions after centuries or millennia of dormancy (e.g. 2010 AD Eyjafjallajökull; 1362 AD Öræfajökull; 3.0 ka, 4.2 ka and 1104 AD Hekla). We present a combined geochemical and geothermobarometric study of magma storage and transfer recorded in the products of the postglacial Búðahraun (~5.0–8.0 ka) and Berserkjahraun (~4.0 ka) eruptions within the Snæfellsnes volcanic zone. The eruption products contain diverse and compositionally heterogeneous macrocryst cargoes recording complex petrogenetic histories of crystal evolution and inheritance from different parts of the sub-volcanic plumbing systems. Geothermobarometry indicates two compositionally and thermally heterogeneous magma storage regions located in the lower (20 ± 4 km) and upper-mid (11 ± 3 km) crust. Crystallization pressure and depth estimates coincide with comparable data from Vatnafell, a small sub-glacial table mountain (tuya) in the centre of the Snæfellsnes volcanic zone, indicating that the nature and conditions of magma storage have remained unchanged since the Upper Pleistocene. Trace element zoning of clinopyroxene macrocrysts indicates that mafic recharge into the upper-mid-crustal storage zone triggered the eruptions of Búðahraun and Berserkjahraun. Evidence for eruption-triggering mafic recharge and basaltic cannibalism involving the transfer and amalgamation of crystals with different evolutionary histories sets the Búðahraun and Berserkjahraun eruptions apart from other studied eruptions in Iceland. We propose that the compositional and textural diversity preserved within the crystal cargoes are a direct consequence of the reduced heat flow beneath the Snæfellsnes volcanic zone, which favours the formation of isolated melt pockets in which compositionally diverse macrocryst populations formed. Periodic flushes of primitive basaltic magma from depth promote widespread mixing with evolved melts,

resulting in the assembly of crystals with diverse ancestries from different parts of the sub-volcanic systems. Insights gained from the diverse macrocryst cargoes of Búðahraun and Berserkjahraun and comparisons with recent off-rift volcanism in Iceland are essential for the development of future monitoring efforts and hazard evaluation. Although volcanism within the Snæfellsnes volcanic zone differs fundamentally from that in rift zones where eruptions are controlled by extensional spreading, magma ascent from depth still appears to follow pre-existing tectonic escape routes. This could result in extremely short advance warning times on the order of a few days.

INTRODUCTION

Modern views of magma storage embrace the concept of vertically extensive transcrustal magmatic systems, consisting of intricate networks of interconnected multi-level magma storage horizons, embedded in variably solidified magmatic mush zones (e.g. Cashman *et al.,* 2017). Mush zones are dynamic bodies containing enough crystals to form a touching framework with interspersed melt lenses of variable shape and size (Cashman *et al.,* 2017; Edmonds *et al.,* 2019); as such, proportions of crystals and melt within these zones vary spatially and temporally. A critical feature of transcrustal magmatic systems is their transient character, which can facilitate the rapid remobilization of large volumes of magma through various crustal storage levels via the successive destabilization of melt lenses (Sparks & Cashman, 2017). This vertical re-organization may take place in response to a tipping point caused by long-term magmatic processes including, e.g. fractionation, compaction, reactive flow, triggering by mafic magma recharge (Tait *et al.,* 1989; Edmonds *et al.* 2019) or through tectonic forcing (Linde & Sacks, 1998; Edmonds *et al.* 2019; Cashman *et al.,* 2017). Establishing the conditions and dynamics of pre-eruptive magma storage and transfer within these transient transcrustal storage networks is a major focus of quantitative volcanic petrology (e.g. Kahl *et al.,* 2011, 2015, 2017; Ubide *et al.,* 2019*a*, 2019*b*; Magee *et al.,* 2020).

In Iceland, geobarometric data indicate that magma storage, evolution and crustal accretion within Icelandic rift-zone volcanic systems occur at a range of depths (5–30 km) spanning the crust and uppermost mantle, with magma processing mainly occurring within networks of decimetre-thick sills (e.g. Hansen & Grönvold, 2000; Neave & Putirka, 2017; Maclennan, 2019; Neave *et al.,* 2019; Caracciolo *et al.,* 2020). Geophysical and petrological data for Iceland are consistent with models of stacked sills, where melts rising from the mantle typically stall at several intermediary tiers within the crust on their way to eruption (Maclennan *et al.,* 2001; Edmonds *et al.,* 2019; Maclennan, 2019; White *et al.,* 2019). Unlike transcrustal mush-dominated magmatic systems (see Cashman *et al.,* 2017), the stacked-sills model suggests that melt lenses are embedded in hot but subsolidus country rock and that the formation of transient mushes is limited to the margins of the sills (Maclennan, 2019).

Volcanic activity in Iceland is not only confined to the axial rift systems, but can also occur within intraplate volcanic belts, the so-called flank zones (Jakobsson, 1972; Sæmundsson, 1978; Einarsson, 1991). In contrast with the on-rift volcanic zones, flank zones are peripheral to the active spreading centres and located in off-rift areas of Iceland (e.g. Einarsson, 2008 and references therein). Whilst the behaviour of on-rift magmatic plumbing systems and the conditions and timescales of magma storage, mixing and transfer within Iceland are increasingly well constrained, relatively little is known about magma dynamics in the off-rift volcanic flank zones. Crucially, off-rift volcanoes can generate hazardous explosive silicic eruptions [e.g. VEI 6: 3 ka (H3) and 4.2 ka (H4) at Hekla; 1362 AD at Öræfajökull; VEI 4–5: 1104 AD (H1) at Hekla] after centuries or millennia in a dormant state (e.g. Thorarinsson, 1958; Steinthórsson, 1967; Thorarinsson, 1967; Larsen & Thorarinsson, 1977; Janebo *et al.,* 2016).

In this contribution, we apply a quantitative petrological approach combining major, minor and trace element geochemistry of mineral and melt phases with geothermobarometry to constrain the dynamic behaviour of magma storage and transfer within two off-rift volcanic systems in the Snæfellsnes volcanic zone (SNVZ), a Tertiary volcanic zone reactivated at 2 Ma and located on the Snæfellsnes peninsula in western Iceland (Fig. 1a). We approach this by studying eruption products from two Holocene (<11.5 ka) eruptions, Búðahraun and Berserkjahraun. We synthesize our findings and results to develop a conceptual model of the Holocene transcrustal magma storage and transfer within two geographically distinct magmatic systems along the SNVZ. Constraining the conditions and dynamics of magma storage and remobilization along the SNVZ is highly relevant, not only for help interpreting future signs of volcanic unrest, but also for assessing the potential hazards linked to rapid magma ascent along pre-existing ascent pathways within one of Iceland's least monitored areas.

GEOLOGICAL CONTEXT

Iceland is an elevated and subaerial part of the northern Mid-Atlantic Ridge located at the junction between
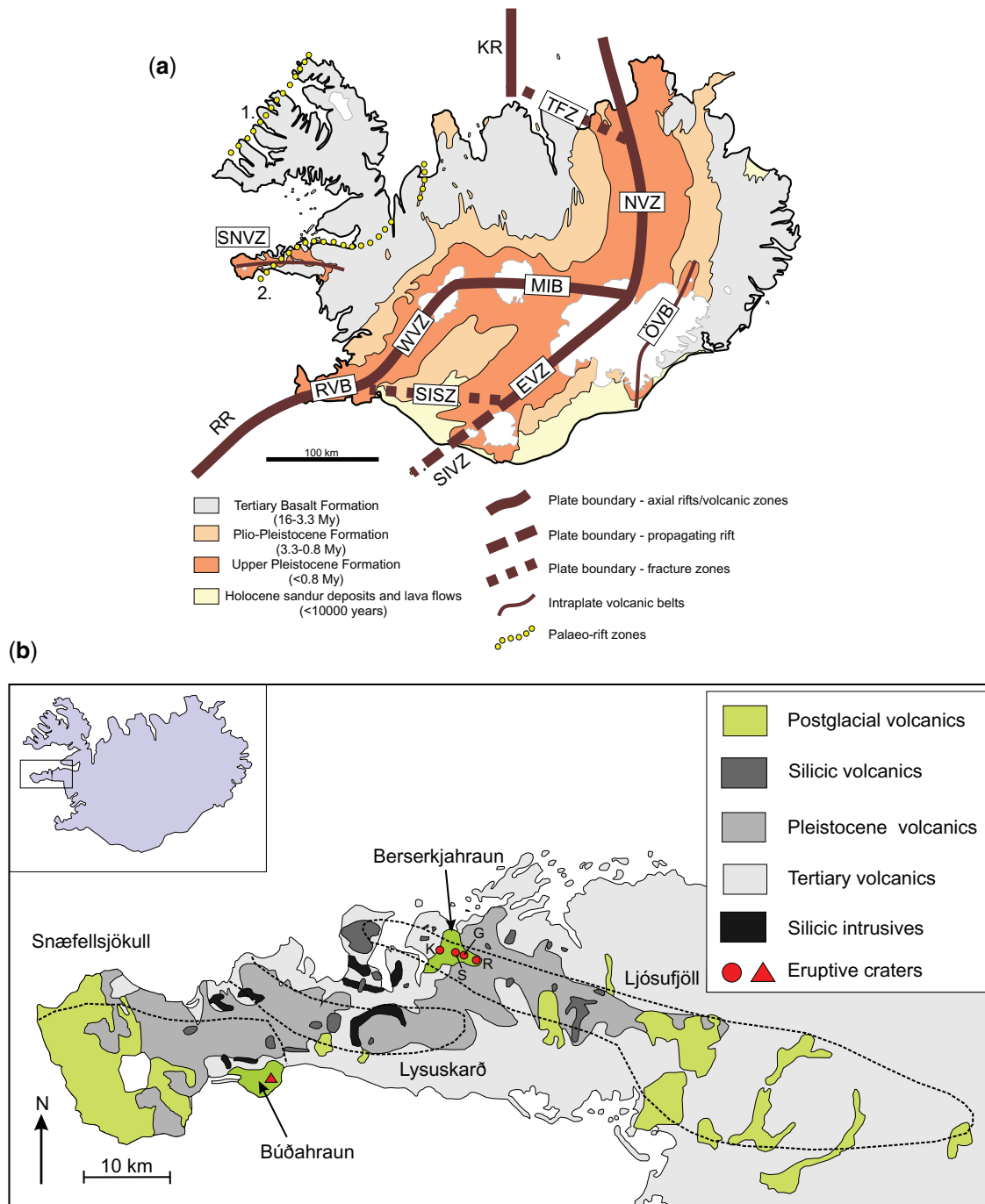
Fig. 1. (A) Overview map detailing principal elements of the geology of Iceland including main fault structures, volcanic zones and belts. RR: Reykjanes Ridge; RVB: Reykjanes Volcanic Belt; SISZ: South Iceland Seismic Zone; SIVZ: South Iceland Volcanic Zone; WVZ: West Volcanic Zone; MIB: Mid-Iceland Belt; EVZ: East Volcanic Zone; NVZ: North Volcanic Zone; TFZ: Tjörnes Fracture Zone; KR: Kolbeinsey Ridge; ÖVB: Öræfi Volcanic Belt; SNVZ, Snæfellsnes Volcanic Zone. Numerals 1 and 2 denote outlines of extinct rift axis in west and north-west Iceland. Figure adapted from Thordarson & Larsen (2007). (B) Simplified geological overview map of the Snæfellsnes peninsula, west Iceland (from Flude *et al.*, 2008). Black dashed lines illustrate the inferred outlines of the three sub-rift volcanic systems: (a) Ljósufjöll, (b) Lýsuskarð and (c) Snæfellsjökull. Filled circles indicate locations of the Berserkjahraun craters: Kothraunskúla (K), Smáhraunskúlur (S), Gráakúla (G) and Rauðakúla (R). Filled triangle: location of the Búðahraun crater, Búðaklettur, within the Snæfellsjökull volcanic system. Black star: location of Vatnafell, a small subglacial tuya (Burney *et al.*, 2020).

Reykjanes Ridge in the south and Kolbeinsey Ridge in the north (Fig. 1a) (e.g. Gudmundsson, 2007). The spreading ridge axis, marking the trace of the divergent plate boundary between the North-American and the Eurasian plates, moved on top of the Iceland mantle plume at ∼24–19 Ma

(magnetic anomaly 6) (e.g. Ward, 1971; Vink, 1984; Óskarsson *et al.*, 1985; Einarsson, 1991; Harðarson, 1993; Harðarson *et al.*, 2008). The divergent plate boundary across Iceland is represented by several tectonically and volcanologically active segments or neovolcanic zones,

including the Northern Volcanic Zone in north Iceland and the two sub-parallel rift zones in south Iceland, the Western and the Eastern volcanic zones (Fig. 1a). Successive eastward jumps of the spreading zones over the past 16 Ma (Harðarson *et al.*, 2008 and references therein) created an unstable regime that led to the formation of complex fracture zones in the north (Tjörnes fracture zone) and south (South Iceland Seismic Zone) accommodating the differential motions of the different plate boundary segments (e.g. Einarsson, 1991; Einarsson, 2008).

Geology of the Snæfellsnes volcanic zone, Western Iceland

Located on the $\sim$80 km long, 10–30 km wide and E–W trending Snæfellsnes peninsula in western Iceland, the SNVZ hosts the largest region of off-rift volcanism in Iceland (e.g. Harðarson, 1993; Burney *et al.*, 2020). The SNVZ is characterized by poorly developed tensional features, relatively low geothermal gradients ($\sim$40–60°C/km) for Iceland and the eruption of alkalic and transitional basalts (e.g. Sigurdsson, 1970; Jakobsson, 1972; Einarsson, 1991; Sigmarsson *et al.*, 1992; Harðarson, 1993; Gudmundsson, 2000). Estimates of crustal thicknesses along the Snæfellsnes peninsula are variable, ranging from $\sim$20–26 km in the west to $\sim$25–29 km towards the east (e.g. Darbyshire, 2000; Du *et al.*, 2002; Foulger *et al.*, 2003; Kumar, *et al.*, 2007). Geologically, the SNVZ consists of a variety of eruption products, which can be divided into three distinct chronological units: (1) Tertiary formation, older than 3.3 Ma, (2) Plio-Pleistocene formation, from 3.3 to 0.8 Ma and (3) Upper Pleistocene and Holocene formations, younger than 0.8 Ma (e.g. Harðarson, 1993; Thordarson & Larsen, 2007). Tertiary eruption products belong to the tholeiitic rock series and were formed within the extinct Snæfellsnes-Húnaflói rift zone (2. in Fig. 1a) that was active between 15 and 6–7 Ma. Plio-Pleistocene and Holocene volcanics were erupted in a non-rifting flank zone environment forming a narrow belt that extends 120 km from Grábrók in the east to the tip of the Snæfellsnes peninsula in the west (Harðarson, 1993). Quaternary eruptive centres along the SNVZ display distinct, NW–SE trending alignments (Fig. 1b) that can be divided into three volcanic systems (e.g. Sigurdsson, 1970; Jóhannesson, 1980, 1982b; Harðarson, 1993): (1) Ljósufjöll to the east, (2) Lýsuskarð in the middle and (3) Snæfellsjökull in the west (Jóhannesson, 1980, 1982b). The three systems are arranged in an *en echelon* fashion, trending almost perpendicular to the main axial rift zone (e.g. Harðarson, 1993), due to a right-lateral transcurrent fault zone running the length of the Snæfellsnes peninsula (e.g. Sigurdsson, 1970; Jóhannesson, 2019; Burney *et al.*, 2020). The presence of WNW-trending *en echelon* fractures hosting Recent and Pleistocene eruptive centres provided pathways for rapid magma ascent between the mantle and the currently active volcanic systems within the SNVZ (e.g. Sigurdsson, 1970; Jóhannesson, 2019). The limited crustal extension results in focussed volcanism, with eruptions taking place from

monogenetic cones and sub-glacial table mountains (tuyas) rather than from elongate fissures (Burney *et al.*, 2020). Except for recent work by Burney *et al.* (2020), who investigated conditions of magma plumbing at Vatnafell, a small sub-glacial ($\sim$410 ka) tuya located within the central Snæfellsnes peninsula, and a study by Kokfelt *et al.* (2009), who assessed critical timescales of magma differentiation at the Snæfellsjökull central volcano, there is currently no integrated view of the nature and dynamics of magma processing within the SNVZ.

Búðahraun and Berserkjahraun

The Búðahraun eruption (Búð) occurred $\sim$5.0–8.0 ka ago from Búðaklettur, a crater SW of Búðir (Fig. 1b) in the Snæfellsjökull volcanic system, the westernmost of the three systems in the SNVZ (e.g. Harðarson, 1993; Jóhannesson, 2019). The Snæfellsjökull volcanic system is $\sim$30 km long and up to 20 km wide, consisting of a central volcano, Snæfellsjökull and an E–W trending fissure swarm. The eastern part of the fissure swarm has produced only one Holocene lava flow, Búðahraun, which covers about $\sim$18 km^2 (Jóhannesson, 2019).

The Berserkjahraun (Bers) eruption occurred $\sim$4.0 ka ago within the $\sim$80–90 km long, $\sim$15–20 km wide WNW–ESE trending Ljósufjöll volcanic system (e.g. Jóhannesson *et al.*, 1981; Jóhannesson, 1982b; Harðarson, 1993). It constitutes the easternmost of three volcanic systems in the SNVZ and consists of a central volcano, Ljósufjöll, and a fissure swarm (e.g. Thordarson & Höskuldsson, 2008; Jóhannesson, 2019). The central volcano is a ridge composed of sub-glacially erupted rhyolitic mountains. Holocene activity is, however, confined to small basaltic eruptions. The fissure swarm has produced numerous ($\sim$17) small basaltic lava flows during the Holocene, the largest covering 33 km^2, and small basaltic tephra deposits (Jóhannesson, 2019). The Berserkjahraun eruption occurred at four craters (Fig. 1b): Kothraunskúla in the west, followed by Smáhraunskúlur, Gráakúla and Rauðakúla towards the east (Sigurdsson, 2014).

SAMPLING AND METHODS

A total of eight lava samples from Búðahraun ($n = 6$) and Berserkjahraun ($n = 2$) were collected. Additionally, fresh and glassy scoria samples ($n = 3$) from Kothraunskúla (K1 and K2), Gráakúla and Rauðakúla (R1) craters from the Berserkjahraun eruption were collected. Scoria from Búðaklettur crater is generally altered and was therefore not analysed for glass and mineral chemistry. The locations of all samples studied are highlighted in Fig. 1b and the sampling locations and global positioning system coordinates are listed in Supplementary Data Table 1 (the complete database is available as an electronic appendix, which may be downloaded from http://www.petrology.oupjournals.org/).

Thin sections of lava and quenched scoria samples from Búðahraun and Berserkjahraun were prepared for

microanalysis. Clinopyroxene and olivine macrocrysts >0.5 mm were hand-picked from crushed lava and scoria samples, mounted in epoxy resin and polished to expose melt inclusions (MIs) at the surface. Clinopyroxene-hosted melt inclusions appeared to be naturally quenched, whereas partially or fully crystallized olivine-hosted MIs were heated to 1180 ± 5°C in a high-temperature furnace for 5 minutes and quenched in cold water immediately afterwards (e.g. Caracciolo *et al.*, 2020). Heated MIs were examined by optical microscopy to check for complete homogenization.

Major and minor elements were analysed in 82 groundmass glasses (Búð: *n* = 60; Bers: *n* = 21), 47 melt inclusion glasses (34 olivine-hosted and 13 clinopyroxene-hosted), 32 plagioclase (Búð: *n* = 10; Bers: *n* = 22), 199 olivine (Búð: *n* = 79; Bers: *n* = 120) and 56 clinopyroxene (Búð: *n* = 39; Bers: *n* = 17) macrocrysts by electron microprobe analysis using the JEOL JXA-8230 instrument at the University of Iceland, the JEOL JXA-8200 instrument at the Johannes Gutenberg Universität Mainz and the Cameca SX-100 instrument at the University of Cambridge. We used an accelerating voltage of 15 kV, beam currents of 10 (plagioclase and glass) to 20 nA (olivine, clinopyroxene, spinel) and beam spot sizes ranging from fully focussed (olivine, spinel) to a diameter of 5 (clinopyroxene, plagioclase, MIs) and 10 μm (glass). A list of primary standards used for calibration, including peak and background count times, are provided in the electronic appendix Supplementary Data Material S1. Precision was estimated by measuring the following standards during each session: USNM 2566 (springwater meteorite) for olivine, NMNH 164905 (Cr-Augite) for pyroxene, Basalt Glass A-99 (USNM 113498–1) from Makaopuhi Lava Lake (Jarosewich, 2002) and Plagioclase (Labradorite) from Sonora, Mexico (Astimex Standard Ltd). Repeated analysis of secondary standards indicate that olivine forsterite content [Fo = $100 \times Mg/(Mg + Fe^{2+})$], clinopyroxene Mg-number [Mg# = $100 \times (Mg/(Mg + Fe_{tot})$] and Plagioclase anorthite content [An = $100 \times Ca/(Ca + Na)$] were determined with 1 sigma precisions of ±0.13 (*n* = 154), ±0.20 (*n* = 79) and ±0.41 mol% (*n* = 25). Major (>1 wt%) and minor (<1wt%) glass contents were determined with precisions better than $1\sigma = \pm5.3\%$ and 16.7%.

Minor and trace element compositions in nine clinopyroxene macrocrysts and the surrounding groundmass were investigated using laser ablation–inductively coupled plasma–mass spectrometry (LA–ICP–MS) at the University of Queensland Centre for Geoanalytical Mass Spectrometry, Radiogenic Isotope Facility (UQ RIF-lab), following the elemental mapping method developed by Ubide *et al.* (2015). The instrument set up combined an ASI RESOlution 193 nm excimer UV ArF laser ablation system with a dual-volume Laurin Technic ablation cell and GeoStar Norris software, and a Thermo iCap RQ quadruple mass spectrometer with Qtegra software. Full instrument details are described in Ubide *et al.* (2019*a*). Ablation parameters included 14×14 μm² square-shaped laser aperture, 14 μm/s

translation speed, 10 Hz repetition rate, 3 J/cm² fluence, 1 μm overlap between ablation lines and 20 s pause after each line to allow washout and monitor the background. Measured analytes were ^{7}Li, ^{27}Al, ^{43}Ca, ^{45}Sc, ^{49}Ti, ^{51}V, ^{52}Cr, ^{60}Ni, ^{88}Sr, ^{90}Zr, ^{93}Nb, ^{139}La, ^{140}Ce, ^{146}Nd, ^{153}Eu and ^{172}Yb, with a total dwell cycle of 165 ms. We analysed NIST612 glass reference material as primary (calibration) standard and BHVO-2G, BCR-2G, BIR-1G and GSD-1G glass reference materials (http://georem.mpch-mainz.gwdg.de/) as secondary standards to monitor precision and accuracy (better than 5 and 5–10%, respectively). Standards were measured using the same analytical conditions as the unknowns, at the beginning and end of each analytical session and before and after each map. For quantification, we used calcium concentrations obtained by electron microprobe as internal standard. Full analytical details are provided in the electronic appendix Supplementary Data Material S1.

All MI compositions were corrected for post-entrapment crystallization (PEC) that took place during natural and experimental quenching. Details on melt inclusion homogenization experiments and PEC corrections are available in the electronic appendix Supplementary Data Material S1.

Crustal storage conditions within the SNVZ were constrained by applying mineral-melt and melt-only geothermometers and geobarometers. Melt inclusion and groundmass glass temperatures were calculated using equation 14 from Putirka (2008), a pressure independent melt composition thermometer that has a standard error of estimate (SEE) of ±51°C. Olivine-melt (SEE = ±44°C) and plagioclase-melt (SEE = ±36°C) temperatures were calculated with equations 22 and 24a from Putirka (2008), using groundmass glass and PEC-corrected melt inclusion compositions. Olivine-melt equilibrium pairs were selected following the criteria outlined in Putirka (2008), i.e. $K_{D\ Fe-Mg}^{ol-liq} = 0.30 \pm 0.03$ (1SEE) assuming 1 wt% H_2O (e.g. Matthews, 2019) and $Fe^{2+}/\Sigma Fe$ ratios of 0.85 (van der Meer *et al.*, in press). Plagioclase-melt equilibrium pairs were selected following the model of Namur *et al.* (2012; equation 33) and were considered to be in equilibrium if measured anorthite values were within ±2 mol% of predicted equilibrium values. Clinopyroxene crystallization pressures and temperatures were calculated using the clinopyroxene-melt barometer of Neave & Putirka (2017; equation 1) coupled with the Jd-DiHd exchange thermometer of Putirka (2008; equation 33). The geobarometer and geothermometer are associated with SEE of ±140 MPa and ±45°C (Putirka, 2008; Neave & Putirka, 2017). Clinopyroxene-melt pairs were filtered carefully for multi-equilibrium tests as outlined in Neave *et al.* (2019). Equilibrium was considered if: (1) $K_{D\ Fe-Mg}^{cpx-liq}$ values were within ±0.03 of equilibrium values (i.e. $K_{D\ Fe-Mg}^{cpx-liq} = 0.27 \pm 0.03$; e.g. Putirka, 2008) assuming 1 wt% H_2O (e.g. Matthews, 2019) and $Fe^{2+}/\Sigma Fe$ ratios of 0.85 (van der Meer *et al.*, in press); (2) observed enstatite-ferrosilite (EnFs), diopside hedenbergite (DiHd) and Ca-Tschermak's (CaTs) components were within

1SEE of predicted values: EnFs: ± 0.05 (equation 7, Mollo et al., 2013); DiHd: ± 0.06 (equation 6, Mollo et al., 2013) and CaTs: ± 0.03 (equation 3.4, Putirka, 1999). A full account of the applied filtering criteria is provided in the electronic appendix Supplementary Data Material S1.

PETROGRAPHY

Lava and scoria samples from Búðahraun and Berserkjahraun are porphyritic basalts (porphyritic index ~ 10–15%) containing macrocrysts of olivine, clinopyroxene and plagioclase, embedded in a fine-grained, vesicular groundmass. Eruption products from Búðahraun display a hypocrystalline and intergranular groundmass, whereas Berserkjahraun samples are characterized by an intergranular to subophitic or glassy groundmass texture. In both cases, the groundmass consists of laths of plagioclase, clinopyroxene, olivine and spinel. The term macrocryst is used to refer to crystals with a minimum long axis length of >0.5 mm (e.g. Thomson & Maclennan, 2013), without genetic implications. Characteristic macrocryst textures are summarized in Fig. 2 and in Supplementary Data Fig. S1.1–1.4.

Plagioclase (An_{52-87}; see Supplementary Data Table 2) forms euhedral to anhedral crystals of variable size, ranging from 0.4–2.8 mm (long axis). Plagioclase macrocrysts display a variety of textures including normal, reverse and oscillatory zoning, but also pervasive dissolution and resorption features (Fig. 2a–c and Supplementary Data Fig. S1.1).

Olivine (Fo_{66-91}; see Supplementary Data Table 3) is mostly sub-hedral with crystal sizes ranging between 0.1 and 2.2 mm (long axis). Normal and complex reverse zoning occurs frequently, and inclusions of spinel (mostly Cr- and Al-rich spinel), titanomagnetite and partially re-crystallized MIs are common. Rare olivine cores are strongly resorbed with coarse sieve textures. Rims are usually anhedral and strongly embayed with dendritic or hopper morphologies. Some olivine rims contain tiny laths of plagioclase microlites from the surrounding groundmass. Occasionally, olivine forms glomerocrysts with clinopyroxene or with other olivines (Fig. 2d–f and Supplementary Data Fig. S1.2).

Clinopyroxene ($Mg\#_{70-88}$; see Supplementary Data Table 4) forms euhedral to subhedral crystals with sizes between 0.3 and 2.5 mm (long axis). Besides pronounced oscillatory and sector zoning, clinopyroxene crystals also display simple normal and complex zoning, the latter with reverse-zoned cores and normal zoning towards the outermost rims. Clinopyroxene cores are anhedral and often display sector and/or patchy zoning. Corroded low-Mg cores are often overgrown by Mg-rich mantles and thin zones of dissolution and re-growth. Rims are anhedral, occasionally sector zoned and may contain plagioclase microlites from the surrounding groundmass. Melt and spinel inclusions are common (Fig. 2g–i and Supplementary Data Fig. S1.3).

Spinel ($Mg\#_{7-80}$; $Cr\#_{6-71}$; see Supplementary Data Table 5) forms euhedral to anhedral crystals of variable size (0.1 to <0.01 mm) that commonly occur as inclusions in olivine, clinopyroxene and rarely in plagioclase. Spinel also occurs in the groundmass and in interstices between adjacent olivine macrocrysts in glomerocrysts. As inclusions in olivine, spinel crystals are usually euhedral to subhedral. At the contact with the groundmass, spinel forms anhedral crystals with strongly sieve-textured margins incorporating plagioclase and clinopyroxene microlites from the surrounding groundmass (Fig. 2d and Supplementary Data Fig. S1.4).

MINERAL AND GLASS COMPOSITIONS

Groundmass glass and melt inclusion compositions

Groundmass glass and PEC-corrected melt inclusion compositions along with whole-rock compositions from literature are presented in Fig. 3 and in Supplementary Data Fig. S1.5 (glass data are provided in Supplementary Data Table 6).

Groundmass glass compositions from Búðahraun and Berserkjahraun show little internal variability but there are differences between the geographically distinct datasets (Fig. 3). Glasses from Búðahraun are slightly more evolved with MgO 4.8–5.8 wt% (median: 5.5 wt%; Supplementary Data Fig. S1.5), $Mg\#_{liq}$ 37–44 (mean: 42) ($Mg\#_{liq} = [Mg/(Mg + Fe^{2+}) \times 100]$), TiO_2 3.7–4.2 wt%, Al_2O_3/TiO_2 3.2–3.7 and TiO_2/K_2O 3.0–3.4, whereas glasses from Berserkjahraun are slightly more primitive with MgO 4.3–6.2 wt% (median: 5.9 wt%; Supplementary Data Fig. S1.5), $Mg\#_{liq}$ 40–54, TiO_2 2.6–3.1 wt%, Al_2O_3/TiO_2 4.8–5.6 and TiO_2/K_2O 1.7–5.0. Geochemical differences are also evident in SiO_2 (Búð: 46.0–47.2 wt%; Bers: 49.0–50.5 wt%;), Al_2O_3 (Búð: 13.4–14.0 wt%; Bers: 14.4–15.2 wt%) and FeO (Búð: 13.0–14.5 wt%; Bers: 9.2–13.0 wt%; Fig. 3a and c; Supplementary Data Fig. S1.5). Both glass datasets have similar CaO contents, which range between 10.4 and 12.2 wt% (Fig. 3d).

Whole-rock compositions (Harðarson, 1993; Kokfelt et al., 2006; Debaille et al., 2009; Peate et al., 2010) do not overlap with groundmass glasses and reflect geochemical variations between geographically diverse sample sets. Whole rocks have a much larger range of MgO (between 8.0 and 13.9 wt%). Búðahraun whole-rock compositions are relatively evolved, with MgO 8.0–10.5 wt%, TiO_2 2.6–3.3 wt%, FeO 11.3–12.4 wt%, Al_2O_3/TiO_2 4.4–5.5 and TiO_2/K_2O 3.3–3.5. In contrast, whole-rock compositions from Berserkjahraun are relatively primitive, with MgO 9.9–13.9 wt%, TiO_2 1.6–2.0 wt%, FeO 9.4–10.9 wt%, Al_2O_3/TiO_2 7.4–8.0 and TiO_2/K_2O 1.9–2.7. CaO contents among the whole-rock datasets are similar with a range of 10.8–11.7 wt% (Fig. 3d).
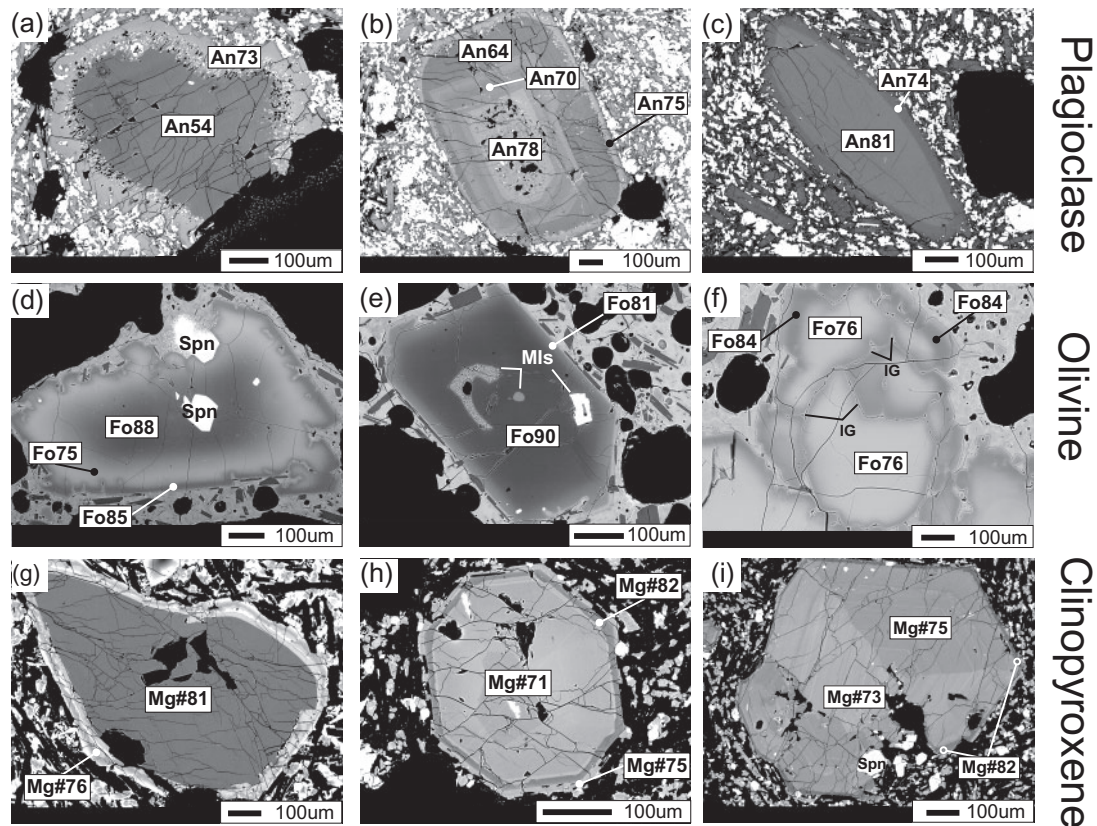
Fig. 2. Backscatter electron (BSE) images of plagioclase (A–C), olivine (D–F) and clinopyroxene (G–I) textures. (A) Reverse-zoned plagioclase with corroded low-anorthite (An_{54}) core overgrown by subhedral anorthite-rich (An_{73}) rim. Note the coarse sieve textures at the contact between the resorbed core and the anorthite-rich rim. (B) Complexly zoned plagioclase consisting of a coarsely sieve-textured, euhedral, anorthite-rich (An_{78}) core followed by a euhedral, oscillatory zoned inner mantle (An_{70}) and a resorbed outer mantle (An_{64}). The contact between outer mantle and rim (An_{75}) is irregular with sieve textures. (C) Normally zoned plagioclase macrocryst containing an ovoidal, anorthite-rich (An_{81}) core followed by an embayed, low-An (An_{74}) subhedral rim. (D) Complexly zoned olivine macrocryst with a high-forsterite (Fo_{88}) core, followed by a low-forsterite (Fo_{75}) mantle, overgrown by a forsterite-rich (Fo_{85}), subhedral outermost rim containing embayments and melt inclusions. Note the development of spinel sieve textures at the margins where spinel is in contact with the groundmass glass. (E) Normally zoned olivine macrocryst with forsteritic (Fo_{90}) core followed by decreasing forsterite contents towards the rims (Fo_{81}). The forsterite-rich core contains naturally quenched and fully crystallized melt inclusions. Olivine rims are usually anhedral, strongly embayed with dendritic or hopper morphologies. Some olivine rims contain tiny plagioclase microlites from the surrounding groundmass. (F) Cluster of reverse-zoned, strongly resorbed olivines with low-forsterite cores (Fo_{76}) followed by forsterite-rich rims (Fo_{84}). Note the occurrence of re-crystallized melt in the interstices between adjacent crystals. (G) Normally zoned clinopyroxene macrocryst with resorbed Mg-rich core ($Mg\#_{81}$) overgrown by an anhedral Mg-poor ($Mg\#_{76}$) rim. The corroded Mg-rich core is surrounded by several zones of dissolution and re-growth (different BSE contrasts). (H) Euhedral, complex reverse-zoned clinopyroxene with a low-Mg core ($Mg\#_{71}$), followed by a Mg-rich mantle ($Mg\#_{82}$) and a low-Mg ($Mg\#_{75}$) outermost rim. The rim contains plagioclase microlites from the surrounding groundmass. (I) Euhedral clinopyroxene macrocryst comprising oscillatory zoning superimposed by hourglass sector zoning overgrown by a thin, Mg-rich outermost rim ($Mg\#_{82}$). Spn: spinel; MIs: melt inclusions; IG: interstitial glass. Anorthite (mol%): $An = 100 \times (Ca/(Ca + Na + K))$; Forsterite content [mol%]: $Fo = 100 \times (Mg/(Mg + Fe^{2+}))$; $Mg\# = 100 \times (Mg/(Mg + Fe_{tot}))$ [mol%].
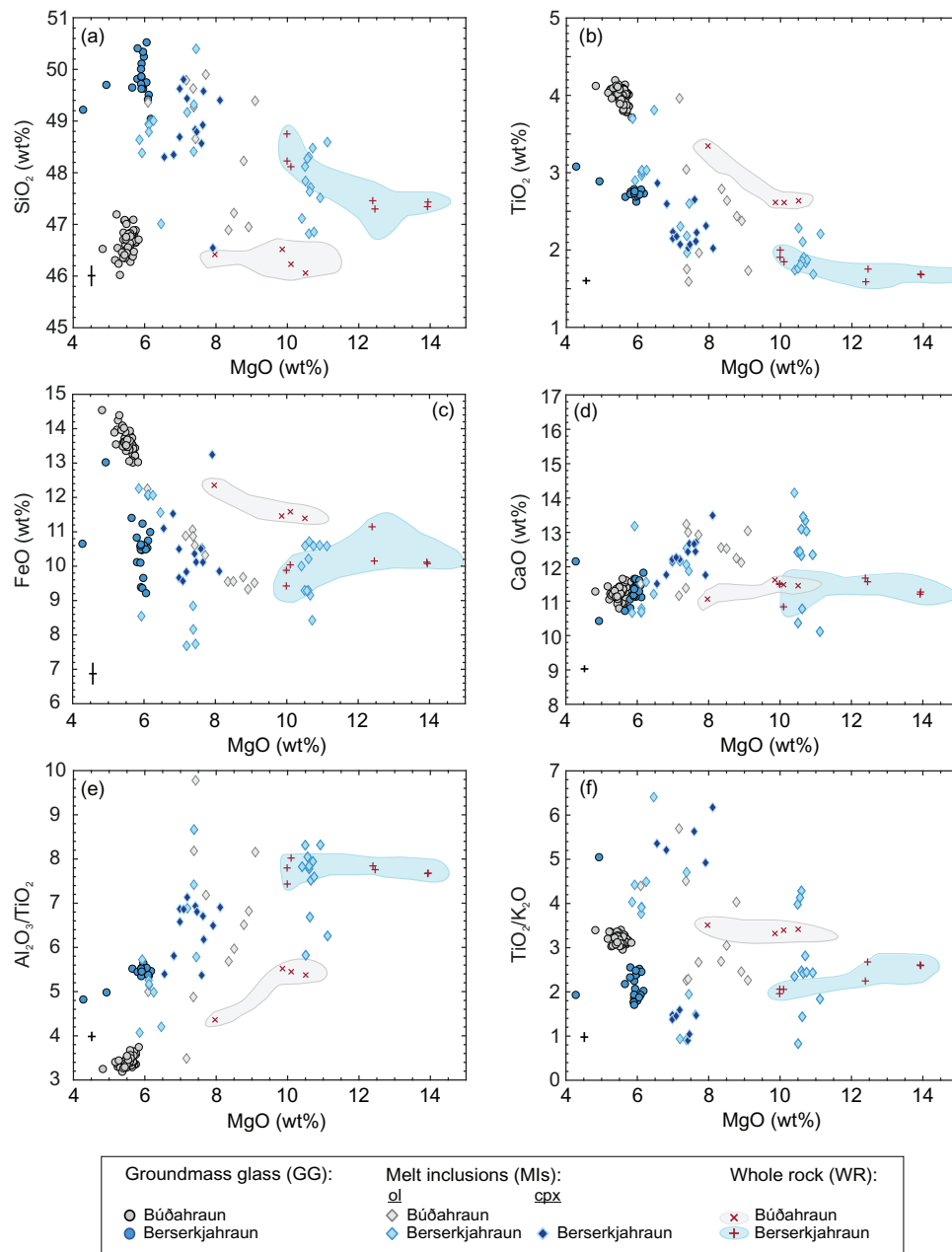
Groundmass glass and whole-rock compositions display negative trends in SiO_2, TiO_2, FeO versus MgO plots and generally low CaO contents, indicating the preferential accumulation of olivine over clinopyroxene and plagioclase in the erupted lavas (Fig. 3a–d).

PEC-corrected olivine- (Fo_{76-90}) and clinopyroxene-hosted ($Mg\#_{82-88}$) MIs are more variable than groundmass glasses and plot at comparatively higher MgO, between 5.9 and 11.1 wt% MgO (median: 7.5 wt%, Supplementary Data Fig. S1.5) with $Mg\#_{liq}$ 46 to 69. Evolved MIs (<6.6 wt% MgO; $Mg\#_{liq}$ 46–51) are hosted within Fo_{76-79} olivines and $Mg\#_{82}$ clinopyroxenes, whereas primitive MIs (MgO 7.0–11.1 wt%, $Mg\#_{liq}$ 54–69) are hosted within Fo_{81-90} olivines and $Mg\#_{82-88}$ clinopyroxenes.

Groundmass compositions in both localities overlap and are enriched in incompatible trace elements relative to compatible ones when normalized to depleted mantle compositions (Salters & Stracke, 2004), with La/Yb_N values between 21.5 and 29.4 (Supplementary Data Fig. S1.6). The overall shape of the groundmass trace element patterns is similar to that of the bulk rock compositions (Peate *et al.*, 2010). However, whole-rock data are slightly less enriched in incompatible elements and more enriched in Ni compared to groundmass values, consistent with the

Fig. 3. Major element versus MgO plots of groundmass glasses, melt inclusions and whole rocks from Búðahraun and Berserkjahraun. Melt inclusion compositions were corrected for post-entrapment crystallization (PEC). Filled circles, groundmass glass compositions; filled diamonds, melt inclusion compositions; grey and turquoise areas, whole-rock compositions. Whole-rock compositions from: Harðarson, 1993; Kokfelt *et al.*, 2006; Debaille *et al.*, 2009; Peate *et al.*, 2010. Error bars (1σ) refer to glass (groundmass and PEC-corrected MIs) compositions from this study.

accumulation of olivine, particularly in the case of Berserkjahraun (Supplementary Data Fig. S1.6b).

Plagioclase

Core and rim compositions of plagioclase macrocrysts from Berserkjahraun ($n = 10$) and Búðahraun ($n = 22$) are shown in Fig. 4. Plagioclase macrocrysts have a diverse

zoning record. Búðahraun plagioclase crystals display normal zoning with high-anorthite cores, followed by low-anorthite rims. Berserkjahraun plagioclases are characterized by both normal and reverse zoning with low- to high-anorthite cores, followed by rims of similar anorthite content (Fig. 2a, c and Supplementary Data Fig. S1.1).

Búðahraun core compositions (An_{75-87}) display a dominant population at An_{84} (Fig. 4a). Berserkjahraun
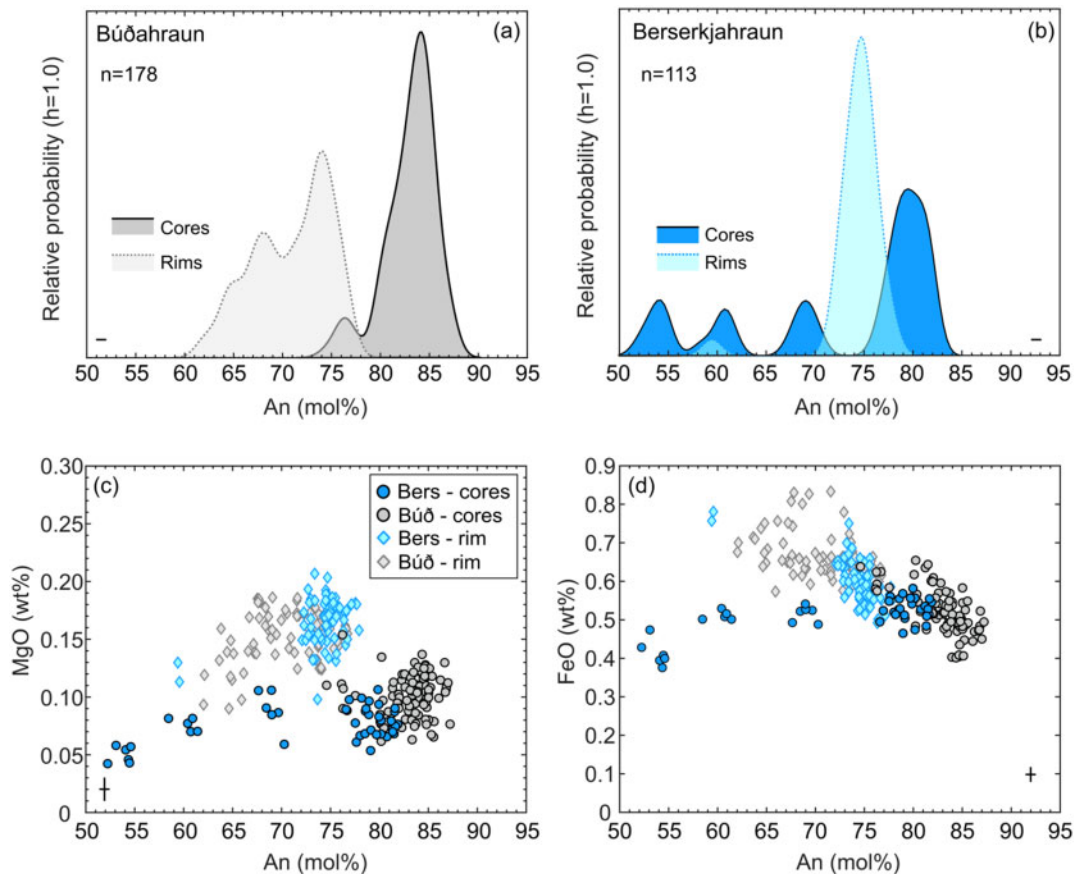
Fig. 4. Major and minor element compositions of plagioclase macrocrysts from Búðahraun and Berserkjahraun. (A, B) Kernel density estimates illustrate anorthite (An) distribution of plagioclase cores and rims. (C, D) MgO and FeO^T versus anorthite content of plagioclase cores and rims. Error bars: 1σ.

core compositions display a multimodal distribution with a dominant population around An_{80} followed by minor modes around An_{54}, An_{61} and An_{69} (Fig. 4b). Búðahraun rim compositions range between An_{62-77} with a subtle peak at An_{74} (Fig. 4a). Berserkjahraun rim compositions range from An_{59-78} with a distinct peak at An_{75} (Fig. 4b).

In FeO and MgO versus anorthite plots (Fig. 4c and d), primitive (An_{75-87}) and evolved (An_{52-70}) plagioclase cores have similar MgO and FeO contents of ≤ 0.1 and 0.4–0.6 wt%, respectively. Rim compositions have higher MgO (0.1–0.2 wt%) and FeO (0.5–0.8 wt%) contents and overlap only partly with the core compositions.
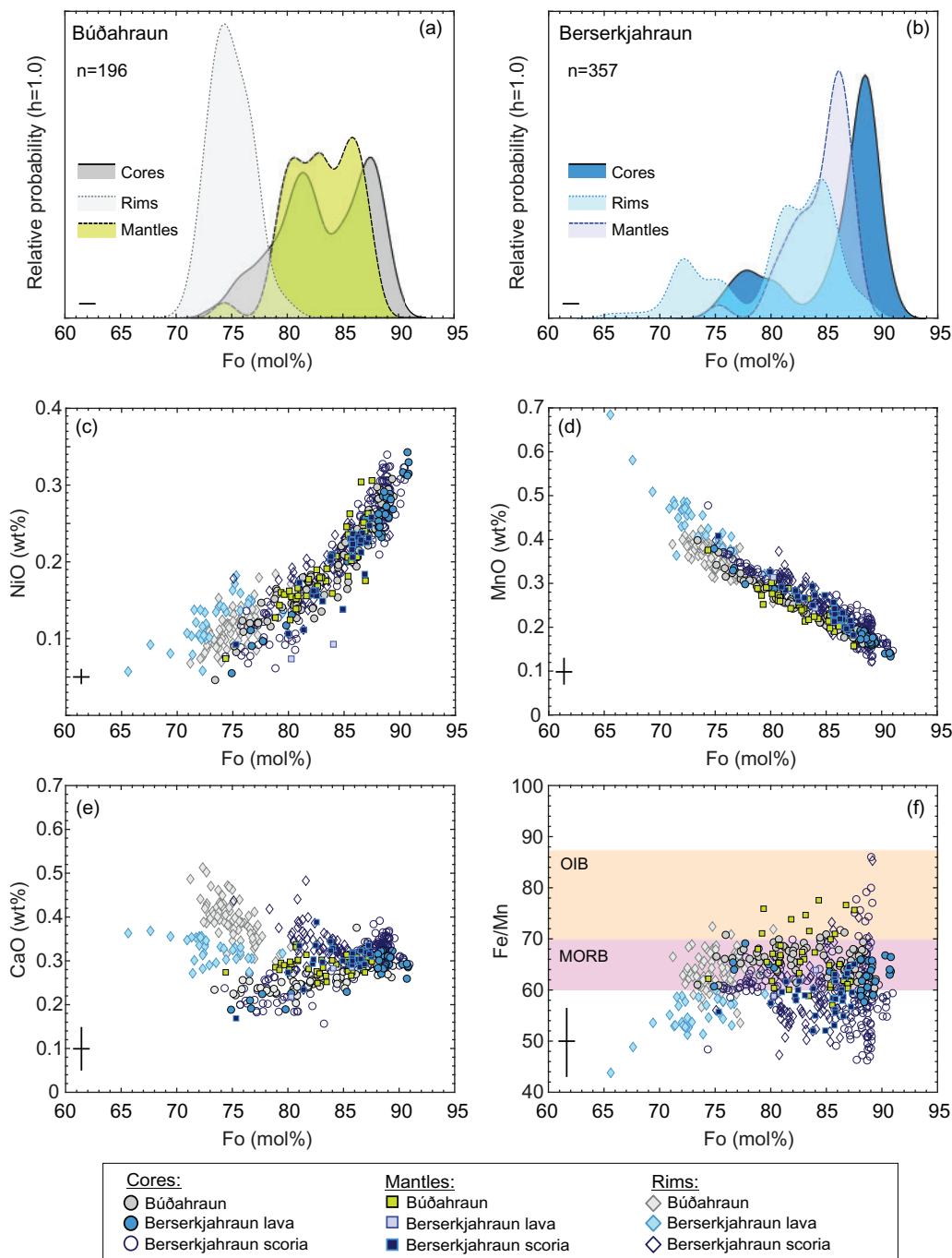
Olivine

Core, rim and intermediate mantle compositions of olivine macrocrysts from Búðahraun ($n = 79$) and Berserkjahraun ($n = 120$) are illustrated in Fig. 5. Olivine core compositions range from Fo_{73} to Fo_{91} (Fig. 5a and b), with bimodality in both cases. Búðahraun core compositions display peaks at Fo_{81} and Fo_{87} (Fig. 5a), whereas core compositions from Berserkjahraun range

between Fo_{74} and Fo_{91}, with a dominant population at Fo_{88} followed by a subsidiary peak at Fo_{78} (Fig. 5b).

Olivine mantles occur between low-forsterite cores and normally zoned outermost rims in complexly zoned olivines (Supplementary Data Fig. S1.2b). Compositionally, olivine mantles from Búðahraun and Berserkjahraun are very similar, and range between Fo_{74} and Fo_{87}, with a distinct peak at Fo_{86} in the case of Berserkjahraun (Fig. 5b). In both cases, olivine mantle compositions partly overlap with core compositions (Fig. 5a and b).

Olivine rim compositions from Búðahraun are unimodal and are in the range Fo_{71-80} with a dominant population around Fo_{74} (Fig. 5a). Berserkjahraun olivine rim compositions show a bimodal distribution with two distinct populations around Fo_{72} and Fo_{85} within a fairly large range of Fo_{66-89} (Fig. 5b). Unlike the cores, rim compositions with $<Fo_{80}$ occur mainly in lava samples, whereas rim compositions with $>Fo_{80}$ are limited to scoria samples (Fig. 5c–f). We believe that the observed bimodality of olivine rim compositions is related to local differences in cooling rates of lava and scoria samples. Rim compositions $>Fo_{80}$ partly overlap with the overall olivine core and mantle compositions from Berserkjahraun (Fig. 5b).

Fig. 5. Major and minor element compositions of olivine macrocrysts from Búðahraun and Berserkjahraun. (A, B) Kernel density estimates (KDEs) depicting forsterite content (Fo) distribution of olivine cores, rims and mantles from Búðahraun and Berserkjahraun lava and scoria. (C–F) NiO, MnO, CaO and Ni/Mn versus forsterite content of olivine cores, rims and mantles. OIB, Ocean Island basalt; MORB, mid-ocean ridge basalt (Sobolev *et al.*, 2007). Error bars, 1σ.

NiO and MnO in olivine cores, rims and mantles define positive and negative correlations with forsterite content, respectively (Fig. 5c–f). Olivine mantles follow the same trends with NiO of 0.1–0.3 wt%, MnO of 0.2–0.4 wt% and CaO of 0.2–0.4 wt%. Olivine rims have NiO contents of 0.1–0.2 wt%, MnO of 0.3–0.7 wt% and CaO of 0.3–0.5 wt%. Mg-rich olivine rims from Berserkjahraun scoria samples plot along the same trend as the cores

and mantles but have higher NiO and lower MnO contents. CaO contents (0.3–0.5 wt%) are particularly high in Fo_{66-78} rims from the lava samples. Fe/Mn ratios vary between 44 and 86 and do not correlate with forsterite content (Fig. 5f).

Besides presenting a heterogeneous and diverse compositional record, the olivines from Búðahraun and Berserkjahraun are also characterized by variable zonation
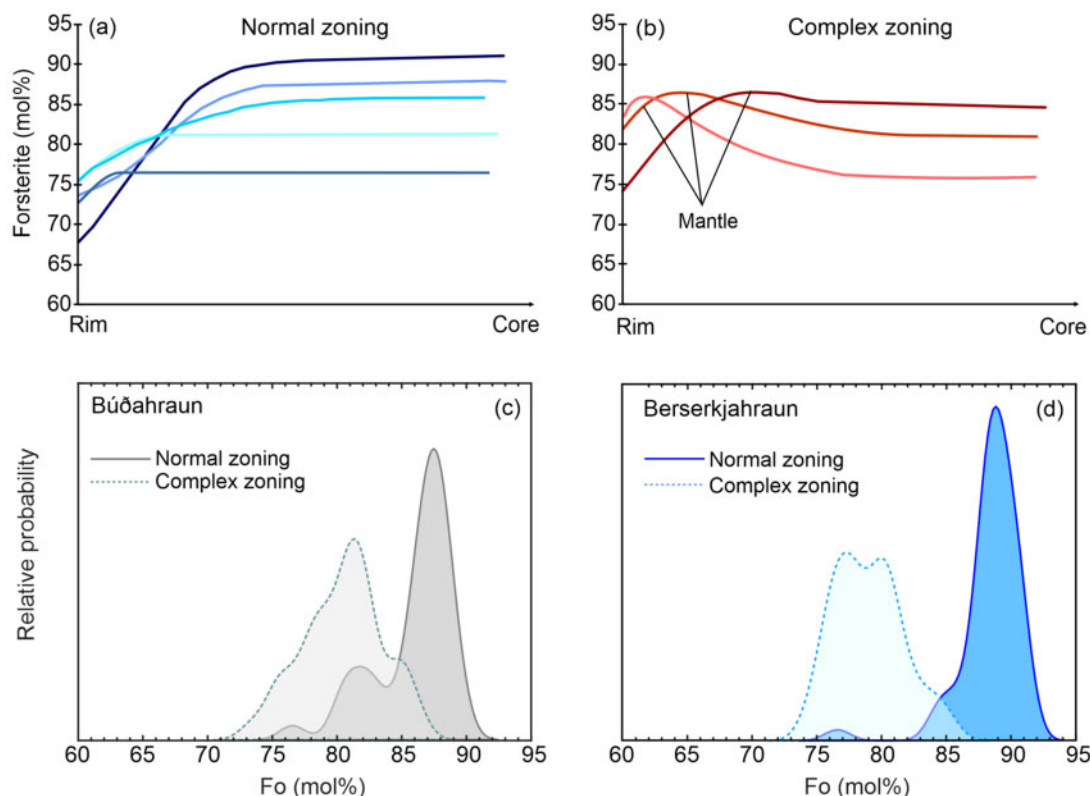
Fig. 6. (A, B) Normal and complex zoning types identified in Búðahraun and Berserkjahraun olivines. Note the occurrence of extended olivine core plateaux of variable composition. (C, D) Kernel density estimates (KDEs) illustrating the forsterite content distribution of olivine core plateaux as functions of normal and reverse zoning types.

senses and patterns (Fig. 6a and b). Normally zoned olivine crystals (53%) are characterized by extensive core plateaux of variable composition (Fo_{76-91}), followed by decreasing forsterite contents towards the rims (Fig. 6a, c and d). Complex zoning patterns (47%), have reverse-zoned crystal interiors of variable composition (Fo_{73-86}), followed by high-forsterite mantles (Fo_{74-87}) and normally zoned outermost rims with decreasing forsterite contents (Fig. 6b–d). Olivines displaying normal zoning are dominated by primitive core compositions ($\sim Fo_{87-89}$), with minor peaks around Fo_{81-82} and Fo_{75-76}. Complexly zoned olivines have more evolved core compositions with peaks around Fo_{77-81} (Fig. 6c and d).
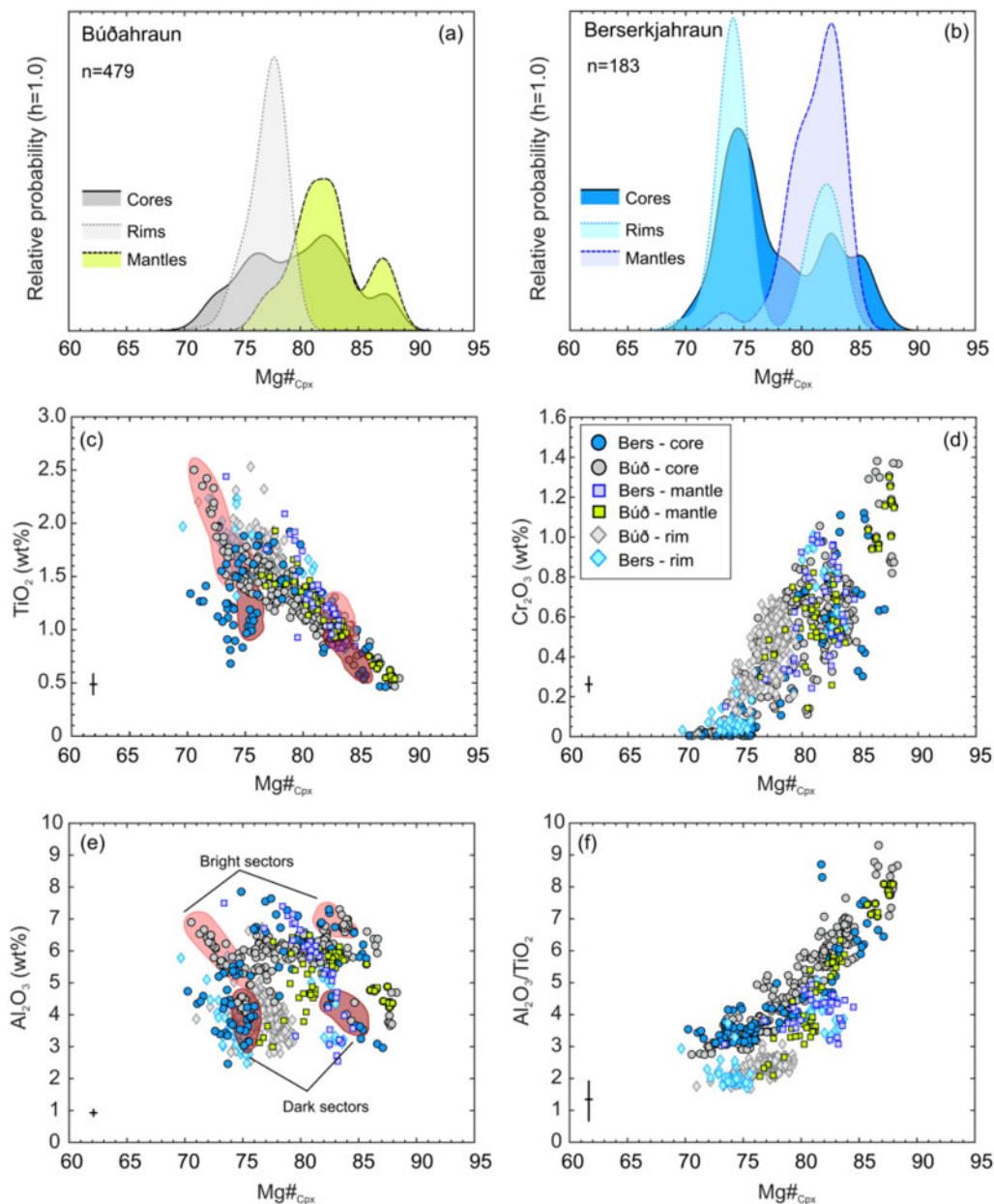
Clinopyroxene

Figure 7 illustrates core, mantle and rim compositions of clinopyroxene macrocrysts from Búðahraun ($n = 39$) and Berserkjahraun ($n = 17$). Core compositions from Búðahraun and Berserkjahraun are very similar and range from $Mg\#_{70}$ to $Mg\#_{88}$ (Fig. 7a and b). Búðahraun core compositions display a single broad peak around $Mg\#_{82}$ (Fig. 7a). Similar to olivine, clinopyroxene core compositions from Berserkjahraun display a bimodal distribution with two distinct populations around $Mg\#_{75}$ and $Mg\#_{82-85}$ (Fig. 7b). $Mg\#_{82-85}$ cores have TiO_2 of 0.5–0.9 wt%, Cr_2O_3

of 0.3–1.4 wt% and Al_2O_3 of 3.0–6.6 wt%. Evolved $Mg\#_{75}$ cores have TiO_2 contents of 0.6–2.5 wt%, Cr_2O_3 of <0.2–1.1 wt% and Al_2O_3 of 2.5–7.8 wt% (Fig. 7c–e).

Mantle compositions of Búðahraun and Berserkjahraun clinopyroxenes are within the range $Mg\#_{73-88}$. Búðahraun mantle compositions display a bimodal distribution with peaks around $Mg\#_{82}$ and $Mg\#_{87}$, while Berserkjahraun mantle compositions display a unimodal distribution with a maximum around $Mg\#_{83}$ (Fig. 7a and b). $Mg\#_{87}$ mantle compositions have TiO_2 of 0.5–0.8 wt%, Cr_2O_3 of 0.7–1.3 wt% and Al_2O_3 of 3.6–5.6 wt%, whereas $Mg\#_{82-83}$ mantle compositions have higher TiO_2 (0.8–2.4 wt%) and Al_2O_3 (2.5–7.5 wt%) and lower Cr_2O_3 (0.1–1.0 wt%) contents (Fig. 7c–e).

Clinopyroxene rims overlap in composition with cores and mantles (Fig. 7a–e; Supplementary Data Fig. S1.7). Rim compositions range from $Mg\#_{70}$ to $Mg\#_{84}$ (Fig. 7a and b). Búðahraun rims display a unimodal distribution between $Mg\#_{71-79}$, with a peak around $Mg\#_{78}$ (Fig. 7a), forming a coherent population with TiO_2, Al_2O_3 and Cr_2O_3 contents ranging between 1.3–2.5, 2.6–6.7 and <0.1–0.7 wt%, respectively. Like clinopyroxene core and olivine core and rim compositions, Berserkjahraun rim compositions also show a strong bimodal distribution between $Mg\#_{70-84}$, with two distinct populations at $Mg\#_{74}$ and $Mg\#_{82}$. $Mg\#_{82}$ rim

Fig. 7. Major and minor element compositions of clinopyroxene macrocrysts from Búðahraun and Berserkjahraun. (A, B) Kernel density estimates (KDEs) showing Mg-number (Mg#) distribution of clinopyroxene cores, rims and mantles. (C–F) TiO_2, Cr_2O_3, Al_2O_3 and $Al_2O_3/TiO2$ versus Mg# of clinopyroxene cores, mantles and rims. Red shaded areas denote sectors with high (bright) and low (dark) BSE intensities. Error bars, 1σ.

compositions have 0.8–1.7 wt% TiO_2, 3.1–6.6 wt% Al_2O_3, (0.2–0.3 wt%) Na_2O and 0.5–1.0 wt% Cr_2O_3, whereas $Mg\#_{74}$ rim compositions have higher TiO_2 (1.3–2.2 wt%) and Na_2O (0.3–1.1 wt%) but lower Al_2O_3 (2.5–5.8 wt%) and Cr_2O_3 (<0.1–0.3 wt%).

Clinopyroxene core, rim and mantle compositions largely overlap, forming continuous negative (TiO_2) and positive (Cr_2O_3 and Al_2O_3/TiO_2) correlations with $Mg\#_{cpx}$ (Fig. 7c–f). Like plagioclase and olivine, clinopyroxene macrocrysts display diverse zoning records including normal, reverse and complex reverse zoning patterns, following variations in Mg# (Fig. 2g and h; Supplementary Data

Fig. S1.3). In addition, clinopyroxenes are characterized by frequent oscillatory and sector zoning, or a combination of the two. Sector zoning affects clinopyroxene cores, mantles and occasionally also the rims (Fig. 2i; Supplementary Data Fig. S1.3). Using backscatter electron (BSE) imaging, sectors with different BSE intensities could be identified. Low-intensity BSE sectors (dark grey) have high $Mg\#_{75-85}$ and Si but low concentrations of Ti and Al (Fig. 7c and e). In contrast, high-BSE intensity sectors (light grey) have lower $Mg\#_{71-84}$ and Si but higher concentrations of Ti and Al (Fig. 7c and e). On the basis of the relationships between zoning geometry and compositional

contrasts (Leung, 1974; Ubide *et al.*, 2019*a*, 2019*b*), we interpret low- and high-BSE intensity sectors as hourglass and prism sectors, respectively. It is reasonable then to assume that some of the overall Ti and Al variability observed in Búðahraun and Berserkjahraun clinopyroxene cores might be caused by subtle sector zoning.

Clinopyroxene trace element chemistry and zoning

Clinopyroxene trace element zoning is illustrated in Fig. 8 and in Supplementary Data Figs S1.8 and S1.9. LA–

ICP–MS maps demonstrate the presence of trace element variability between clinopyroxene macrocrysts from Búðahraun and Berserkjahraun, as well as sharp trace element zonation within individual clinopyroxenes from both localities.

Complex and reverse-zoned clinopyroxenes usually have anhedral and resorbed low-Mg-number cores with high Na_2O contents (Supplementary Data Fig. S1.7), usually followed by high-Mg-number mantles or outermost rims (Fig. 8). Some complexly zoned clinopyroxenes display oscillatory zoned mantles with alternating
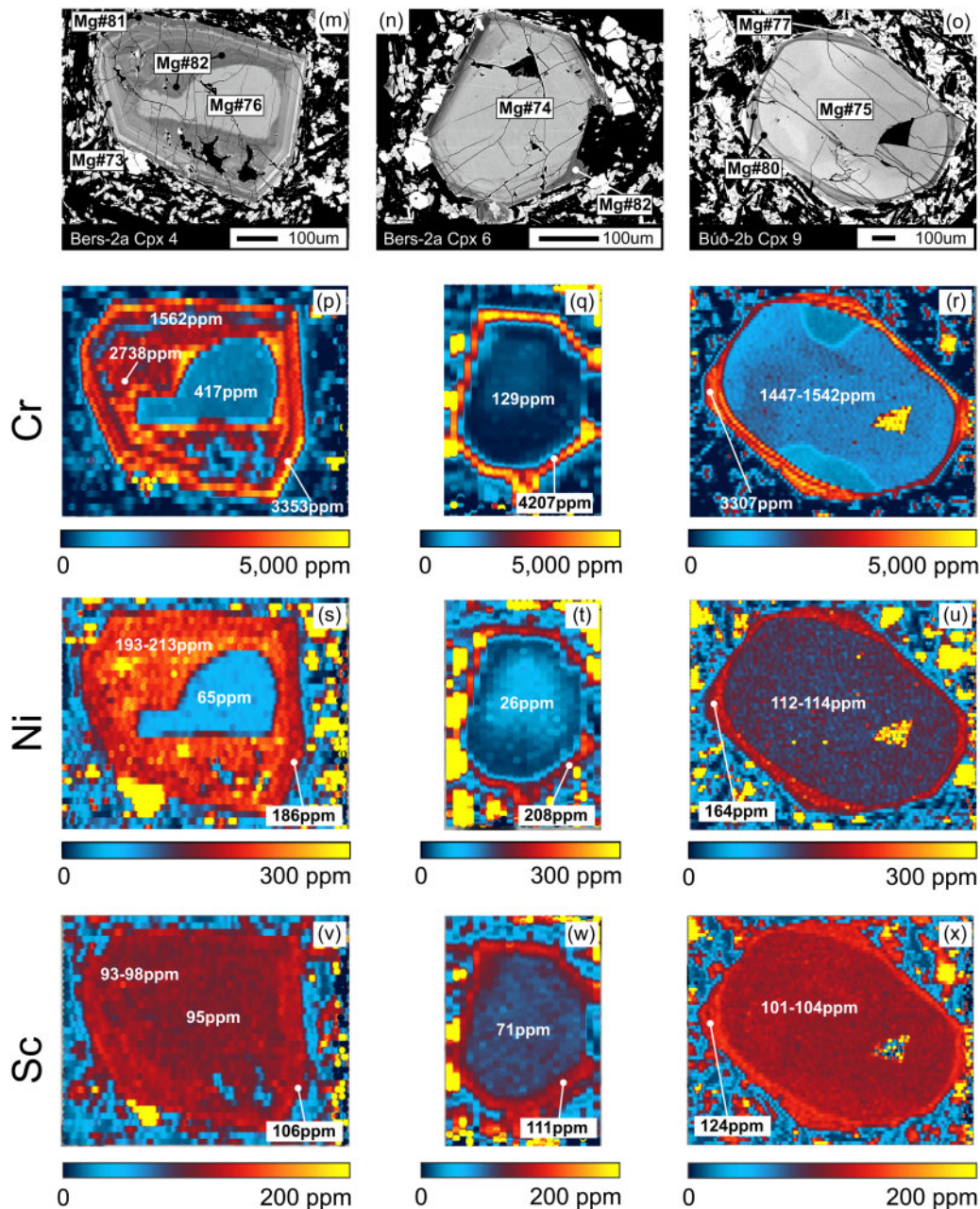
Fig. 8. Trace element maps of clinopyroxene macrocrysts from Búðahraun and Berserkjahraun. (A–C) and (M–O) Backscatter electron (BSE) images. (D–L) and (P–X) Distribution maps of compatible transition metals Cr, Ni and Sc. All maps are quantitative for clinopyroxene and semi-quantitative for other phases. Maps are colour coded with warmer colours indicating higher concentration levels on linear scales within the indicated limits (Ubide & Kamber, 2018). Note that some crystals display multiple zones of Cr and Ni enrichment (F, P). Sector zoning is incipient in Sc (K, L) and well developed in REE-HFSE (Supplementary Data Figs. S1.8 and S1.9), as expected from their high ionic potential (Ubide *et al.*, 2019*a*).

Mg-rich (low BSE intensity) and Mg-poor zones (high BSE intensity) (Fig. 8 c and m), linked in some cases to sector zoning (Fig. 8b and c). LA–ICP–MS maps demonstrate that Mg-rich mantles and rims have prominent enrichments in Cr (1600–4500 ppm) that correlate positively with other compatible transition metals, such as Ni and Sc (Fig. 8 d-x), and are negatively correlated with incompatible elements such as La, Nd and Zr (Supplementary Data Fig. S1.8). Complexly zoned clinopyroxenes with oscillatory zoned mantles exhibiting alternating high- and low-Mg-number zones also show correlated oscillations in Cr. The level of Cr enrichment within these zones is similar to the Cr contents of the outermost rims (Fig. 8 p). In contrast, anhedral and low-

Mg-number cores are low in Cr (<2000 ppm) and Ni (<150 ppm) and relatively enriched in La, Nd and Zr (Supplementary Data Fig. S1.8 and Table 7).

Besides complex and reverse-zoned clinopyroxenes, we also find normally zoned crystals (Supplementary Data Fig. S1.9) with anhedral and resorbed Mg-rich cores that are strongly enriched in Cr (5000–8000 ppm) and Ni (>200 ppm) with Cr levels exceeding those of the Cr-rich mantles and outermost rims of complex and reverse-zoned clinopyroxenes (Supplementary Data Table 7). The Cr-rich cores show complex internal textures, including hourglass and patchy zoning (Supplementary Data Fig. S1.9). The rims are euhedral to subhedral and relatively Cr-poor (2000–3000 ppm),
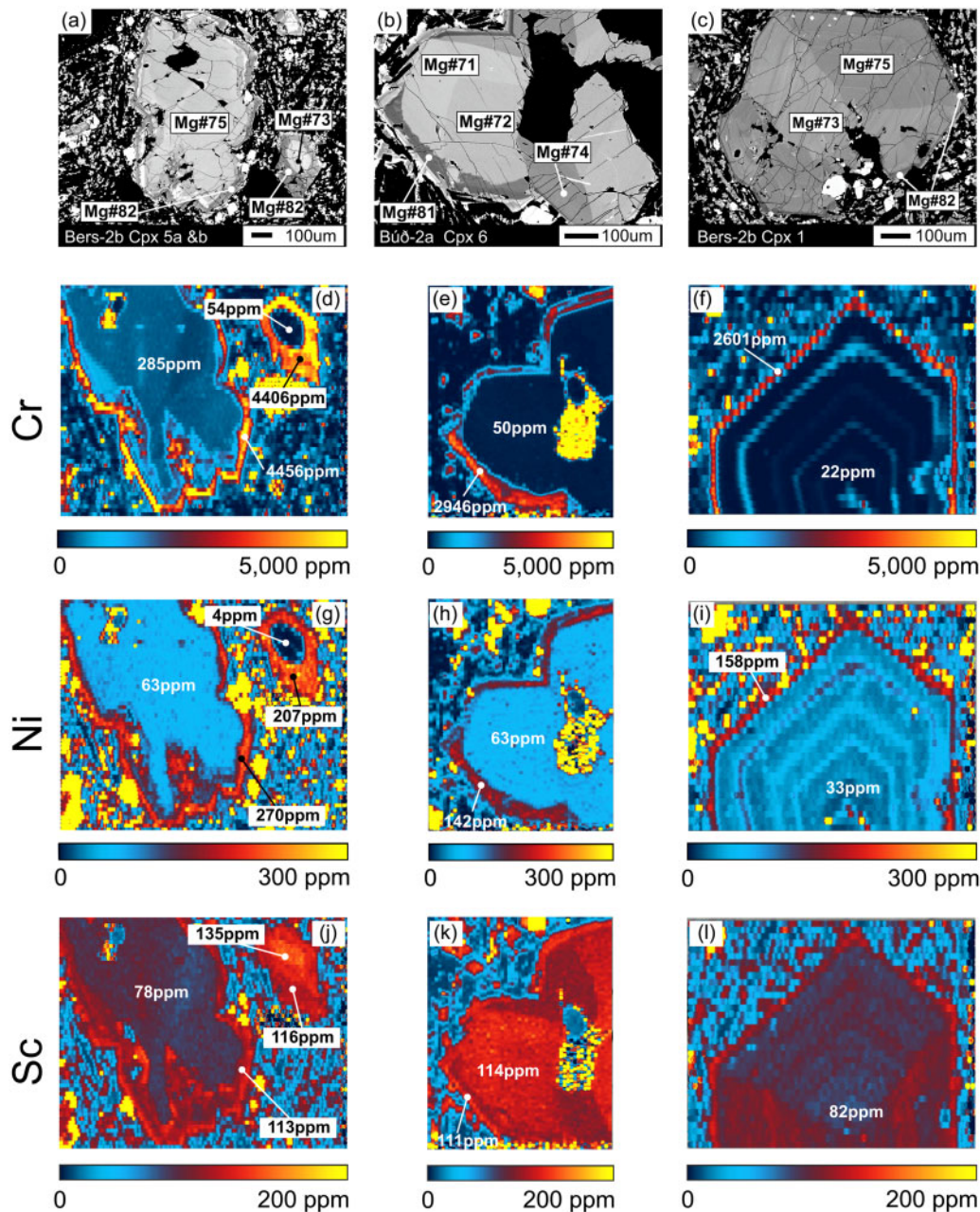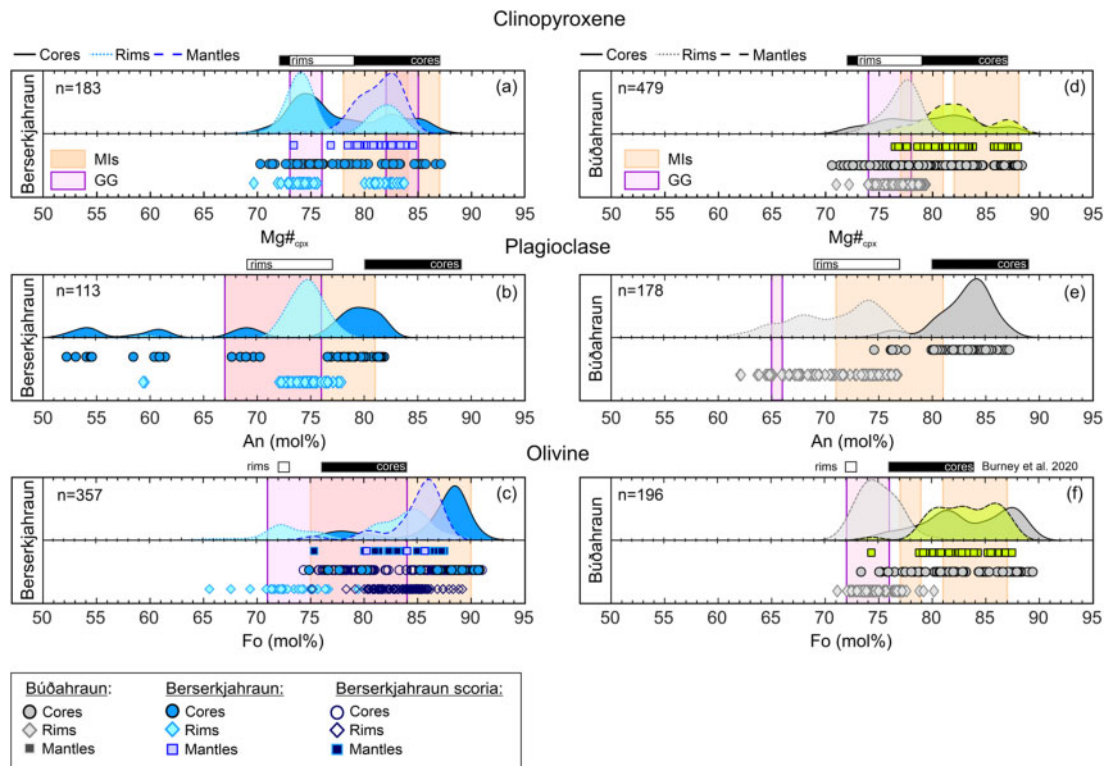

Fig. 8. (continued)

Fig. 9 Mineral-melt equilibrium relations. (A, D) Compositional range of clinopyroxene, (B, E) plagioclase and (C, F) olivine macro-crysts from Búðahraun and Berserkjahraun. Vertical bars show macrocryst compositions in equilibrium with groundmass glass (pink) and melt inclusion (orange) compositions. GG, groundmass glass; MIs, melt inclusions. KDEs of mineral compositions were calculated using a bandwidth of 1.0. White and black boxes labelled cores and rims, show the range of clinopyroxene, plagioclase and olivine macrocryst compositions of eruption products from the sub-glacial Vatnafell tuya in the central part of the Snæfellsnes peninsula (see Fig. 1b) with data from Burney *et al.* (2020) for comparison.

comparable with the rim concentrations of complex and reverse-zoned clinopyroxenes (Fig. 8d–f, and p–r; Supplementary Data Table 7). Scandium behaves differently from Cr and Ni, with lower Sc contents in the cores and increasing Sc contents towards the outermost rims (Supplementary Data Fig. S1.9).

All clinopyroxenes are slightly enriched in light rare earth elements relative to heavy rare earth elements, with an average La/Yb$_N$ of 3.8 in Búðahraun and 3.9 in Berserkjahraun (Supplementary Data Fig. S1.10). On average, clinopyroxene cores in both localities have lower La/Yb$_N$ (Búð: 3.2; Bers: 3.5) than mantles (Bers: 3.8) and rims (Búð: 4.5, Bers: 4.8). Importantly, differences in trace element contents of consecutive zones of individual clinopyroxenes, and between different clinopyroxene macrocrysts from the same locality, cannot be attributed to sector zoning as the overall compositional range in all trace elements is much larger than the differences between different sectors (grouped into squares in Supplementary Data Fig. S1.10c and d).

MINERAL-MELT RELATIONSHIPS

Groundmass glasses were used to investigate crystal-melt relationships and to test whether given macrocryst populations were in chemical equilibrium with their respective

carrier melts at the time of eruption. Figure 9 illustrates the range of olivine, plagioclase and clinopyroxene compositions calculated to be in equilibrium with groundmass glasses (violet vertical bars) from Búðahraun and Berserkjahraun. Predicted mineral-melt equilibrium compositions are provided in Supplementary Data Table 8. Equilibrium compositions were calculated using the model of Namur *et al.* (2012; equation 33) for plagioclase, and the model of Roeder & Emslie (1970) assuming a constant $K_D^{ol-liq}{}_{Fe-Mg}$ of 0.30 ± 0.03 (1SEE) for olivine. Clinopyroxene equilibrium compositions were calculated following the multi-equilibrium tests outlined in Neave *et al.* (2019). A full account of the applied equilibrium criteria and threshold values are given in the methods section and in the electronic appendix Supplementary Material S1. Rare earth element (REE) compositions of basaltic liquids in equilibrium with successive clinopyroxene zones (i.e. cores, mantles and rims) were calculated using the lattice strain model of Wood & Blundy (1997) and were compared to the REE contents of the groundmass as a further test for equilibrium (Fig. 10).

Most macrocryst rims (71%) from Berserkjahraun and Búðahraun appear to be in equilibrium with their respective carrier liquid compositions (Mg#$_{liquid}$ 40–54). Most clinopyroxene cores (67%) and mantles (67%) are, however, too primitive to be in equilibrium with the carrier liquid (Fig. 9a–c). To place constraints on possible
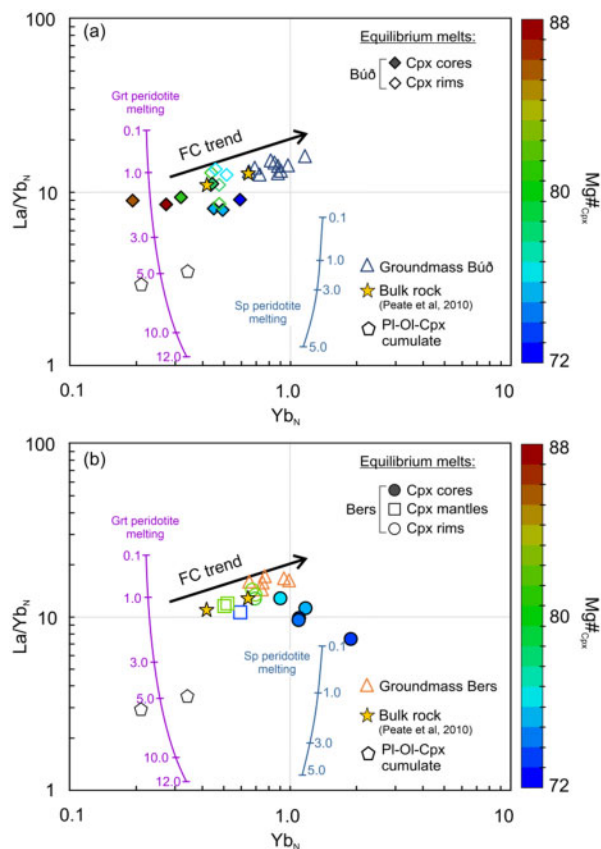
Fig. 10. La/Yb$_N$ versus Yb$_N$ for clinopyroxene equilibrium melts from (A) Búðahraun and (B) Berserkjahraun. Equilibrium melt compositions were calculated for different clinopyroxene segments (i.e. cores, mantles and rims) using the method of Wood & Blundy (1997). Calculated melt compositions were normalized to N-MORB (Hart *et al.*, 1999). Each symbol represents an equilibrium melt composition calculated for a specific clinopyroxene segment. Symbol colours correspond to the Mg-number of the respective clinopyroxene segment. Note, respective error bars are smaller than the symbol sizes. Melting curves of garnet (Grt) and spinel (Sp) peridotite mantle (using depleted MORB mantle compositions of Workman & Hart, 2005) are added. Melting curves were calculated via non-modal batch partial melting assuming 53% olivine, 27% orthopyroxene, 17% clinopyroxene and 3% spinel for spinel peridotite and 60% olivine, 20% orthopyroxene, 15% clinopyroxene and 5% garnet in the garnet peridotite source. Melting modes were 31% orthopyroxene, 63% clinopyroxene and 6% spinel for spinel peridotite, and 7% olivine, 68% orthopyroxene and 25% garnet for garnet peridotite, based on the melting reactions of Kinzler & Grove (1992) and Walter (1998), respectively. Numbers next to the curves indicate degrees of melting. FC trend denotes the fractional crystallization trend calculated assuming an equal amount of plagioclase, clinopyroxene and olivine in the cumulate phase. Pentagons show compositions of plagioclase-clinopyroxene-olivine cumulate at low degrees of melting.

parental melts, we used mineral-melt inclusion partitioning data to assess potential equilibrium relationships. Macrocryst compositions calculated to be in equilibrium with PEC-corrected melt inclusion compositions are depicted as orange vertical bars in Fig. 9. The bulk of Berserkjahraun and Búðahraun cores (69%), mantles (95%) and rims (65%) are close to equilibrium with PEC-corrected MIs (Mg#$_{liquid}$ 46–69).

Most observed macrocryst cores, mantles and rims may have crystallized from groundmass glass and PEC-corrected melt inclusion compositions from Berserkjahraun and Búðahraun. However, a small percentage of plagioclase (11%) and olivine (3%) macrocryst cores are found to be too primitive to be in equilibrium with the observed range of glass compositions (Mg#$_{liquid}$ 40–69). In addition, rare (5%) plagioclase (<An$_{67}$; Fig. 9b) and clinopyroxene (<Mg#$_{73}$; Fig. 9a and d) cores appear to have crystallized from melts more evolved than the observed range of glass compositions. We also find core, mantle and rim compositions that plot within the observed range of glass compositions but for which no equilibrium compositions were found (e.g. Fig. 9a, and d–f). We believe that these macrocrysts may have grown from different melts, not covered by the comprehensive glass (groundmass and MIs) data set presented in this study.

The combined mineral-melt relationship data allows us to classify phenocrystic (in chemical equilibrium with the carrier liquid) and antecrystic (not in chemical equilibrium with the carrier liquid but originated in the same magmatic system; e.g. Streck, 2008; Davidson *et al.*, 2007) mineral populations. Most Berserkjahraun and Búðahraun macrocryst rims (71%) represent phenocrystic material, whereas macrocryst cores (73%) and mantles (77%), represent antecrystic material, either too evolved or too primitive to be in equilibrium with the carrier liquid, suggesting that they were assembled from different regions of the plumbing system. Even though antecryst populations are out of equilibrium with the carrier liquid, they appear to be in equilibrium with a range of melt inclusion compositions.

To test if antecrystic material is related to melts from the same magmatic system by fractionation along a liquid line of descent, we plotted La/Yb$_N$ versus Yb$_N$ (normalized to N-MORB, Hart *et al.*, 1999) of calculated clinopyroxene equilibrium melt compositions for Búðahraun and Berserkjahraun and compared them to bulk rock and groundmass compositions (Fig. 10a and b). All calculated clinopyroxene equilibrium melt compositions cover a narrow La/Yb$_N$ range with an average of 10.7 ± 2 (1σ). This value partly overlaps with those measured in the groundmass (16.1 ± 6.2, 1σ). In line with published studies (e.g. Harðarson & Fitton, 1991; Nikkola *et al.*, 2019a; Rasmussen *et al.*, 2020), this suggests that clinopyroxene equilibrium melt compositions may be derived from a common depleted garnet peridotite mantle source that underwent slightly variable degrees of melting. In contrast, the Yb$_N$ content of calculated equilibrium melts varies by an order of magnitude (0.19 to 1.89), indicating that the clinopyroxene cores, mantles and rims crystallized from variably evolved melts, probably within different parts of the plumbing system.

GEOTHERMOMETRY AND GEOBAROMETRY

Crystallization temperatures

Kernel density estimates (KDEs) showing glass-only and mineral-melt temperature distributions for Búðahraun and
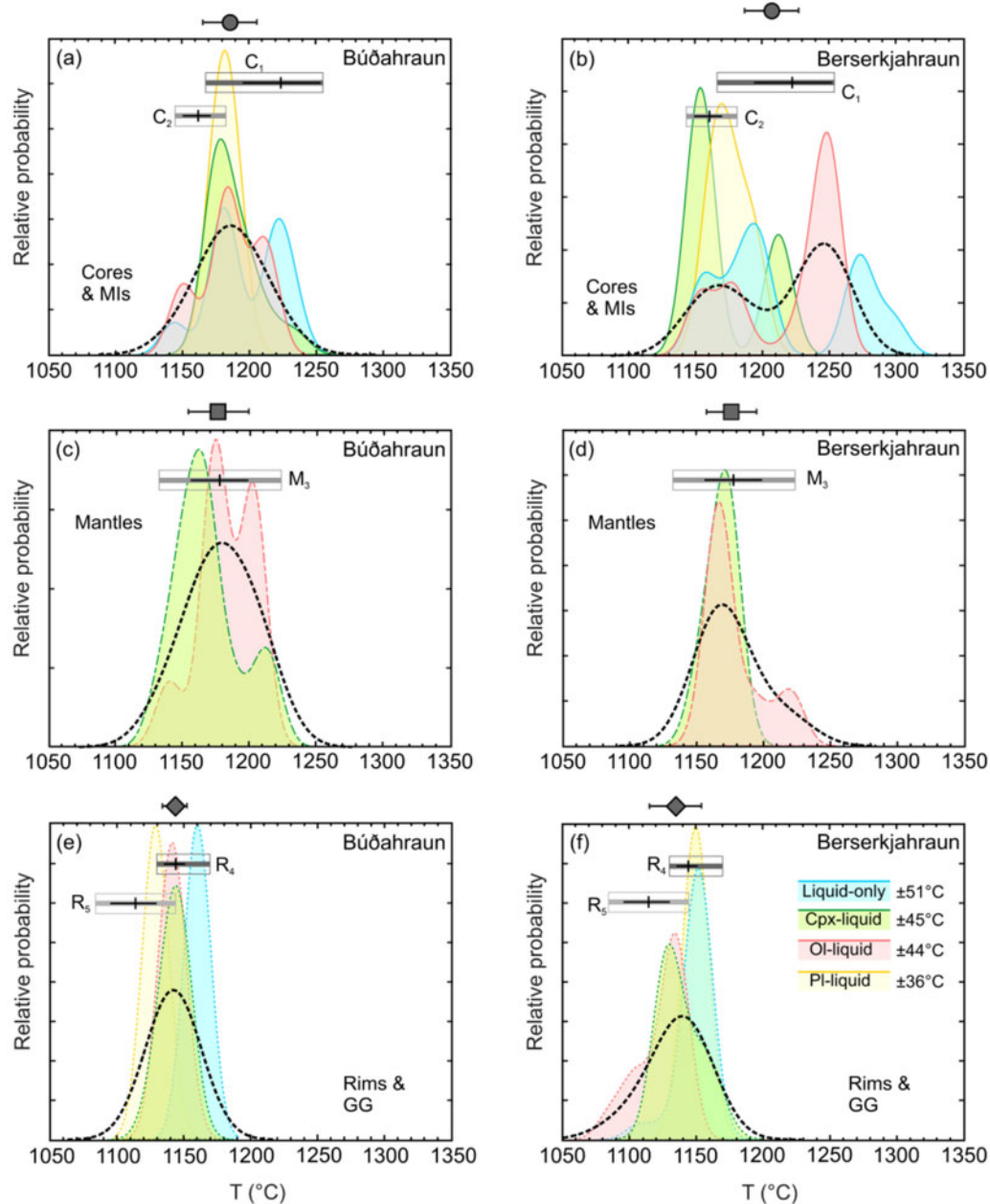
Fig. 11. Kernel density estimates (KDEs) showing temperature distributions from mineral-melt (olivine-melt, clinopyroxene-melt and plagioclase-melt) and melt-only thermometry for macrocryst cores, rims, mantles and glasses (melt inclusions and groundmass) from Búðahraun (A, C, E) and Berserkjahraun (B, D, F). KDEs were calculated using a bandwidth of 10°C. Black stippled KDEs depict combined temperature distribution results for mineral-melt thermometers using a bandwidth of 20°C. Grey symbols above each graph show the mean values for each population, black bars refer to 1σ errors. Boxes denote temperature ranges and mean values of the core (C_1 and C_2) mantle (M_3) and rim (R_4 and R_5) environments.

Berserkjahraun are summarized in Fig. 11. Temperature data are provided in Supplementary Data Table 9. Although Búðahraun and Berserkjahraun erupted from two, widely ($\sim$30 km) separated volcanic systems along the SNVZ, their macrocryst and glass compositional records return similarly complex thermal histories.

Macrocryst cores from Búðahraun and Berserkjahraun record overall temperatures of 1146–1254°C (Fig. 11a and b). KDEs display complex temperature distributions with primitive cores (Fo$_{81-90}$; Mg#$_{79-88}$; An$_{79-82}$) recording

temperatures of 1223 $\pm$ 29°C, and evolved core compositions (Fo$_{76-81}$; Mg#$_{73-78}$; An$_{68-78}$) giving temperatures of 1161 $\pm$ 11°C (C_1 and C_2 in Fig. 11a and b). Glass temperatures are consistent with mineral-melt temperatures recording 1224 $\pm$ 42°C for primitive MIs (Mg#$_{liquid}$ 54–69) and 1157 $\pm$ 9°C for evolved MIs (Mg#$_{liquid}$ 46–51).

Macrocryst mantles (Fo$_{79-87}$; Mg#$_{77-86}$) record temperatures within the range 1132–1224°C (Fig. 11c and d) with mean values of 1178 $\pm$ 22°C for Búðahraun and 1177 $\pm$ 19°C for Berserkjahraun.

Macrocryst rims record the lowest overall temperatures of 1084–1169°C (Fig. 11e and f) with means of 1142 ± 7°C for Búðahraun and 1134 ± 18°C for Berserkjahraun. KDEs for Berserkjahraun rims display, similar to the macrocryst cores, complex thermal histories with primitive rims (Fo_{77-84}; $Mg\#_{79-83}$; An_{73-76}) giving 1143 ± 8°C and evolved macrocryst rims (Fo_{71-76}; $Mg\#_{74-76}$) recording 1113 ± 17°C (R_4 and R_5 in Fig. 11e and f). Groundmass glass temperatures are consistent with macrocryst rim temperatures recording 1118 ± 11°C for evolved ($Mg\#_{liquid}$ 40–42) and 1152 ± 3°C for less evolved ($Mg\#_{liquid}$ 47–54) glass compositions. Lower temperatures recorded by the macrocryst rims could arguably reflect crystallization due to cooling within the lava flows after emplacement. However, olivine rims (Fo_{75-84}) from Berserkjahraun scoria samples were found to record temperatures within the range 1088–1142°C [1133 ± 8°C], underpinning the observed overall cooling trend.

Using a multiple geothermometric approach makes it possible to identify distinct magmatic environments in which the macrocryst cores, mantles and rims formed (e.g. Kahl *et al.*, 2011). Macrocryst cores record the highest temperatures, consistent with melt inclusion temperatures indicating core formation within hotter and possibly deeper parts of both plumbing systems. Macrocryst cores display, however, bimodal composition and temperature distributions, with evolved (mostly phenocrystic) core compositions returning lower temperatures than primitive (antecrystic) cores. The observed temperature difference among the two core populations suggests diverging pre-eruptive growth histories within two thermally distinct magmatic environments, a hotter environment C_1 and a slightly cooler environment C_2 (see Fig. 11a and b). Macrocryst rims return the lowest overall temperatures, consistent with groundmass glass temperatures, indicating that the rims formed within cooler and possibly shallower parts of both plumbing systems. Macrocryst mantles, commonly identified in complex and reverse-zoned olivines and clinopyroxenes, return higher temperatures, indicating that the mantles formed in a hotter environment (M_3) than the rims (Fig. 11c and d). The mantle environment partly overlaps with the two core environments C_1 and C_2 (Fig. 11a and b). We cannot discern if M_3 constitutes a separate environment from thermometric calculations alone. Similar to macrocrysts cores, rims from Berserkjahraun also show bimodal composition and temperature distributions with evolved rims returning lower temperatures than primitive rims. As for macrocryst cores, compositional bimodality in macrocryst rims suggests distinct pre-eruptive growth histories within two thermally distinct environments, R_4 and R_5 (Fig. 11e and f). In Búðahraun, only the slightly hotter rim environment R_4 was identified (Supplementary Data Table 9).

On the basis of the combined compositional and thermal record, we can infer the existence of at least five different magmatic environments involved in the assembly of the heterogeneous Búðahraun and Berserkjahraun macrocryst cargoes. In addition to the thermal differences recorded by adjacent crystal populations (i.e. evolved versus primitive), we also observe an overall cooling trend recorded by successive growth regions (cores → mantles → rims), indicating decreasing temperatures with macrocryst growth (Fig. 11; Supplementary Data Table 9).

Clinopyroxene crystallization pressures

Kernel density estimates (KDEs) showing clinopyroxene-melt crystallization pressure (Neave & Putirka, 2017) distributions for Búðahraun and Berserkjahraun cores, mantles and rims are illustrated in Fig. 12 and calculated pressures are provided in Supplementary Data Table 10.

Evolved ($Mg\#_{73-78}$) and primitive ($Mg\#_{79-88}$) clinopyroxene cores from Búðahraun and Berserkjahraun record overlapping crystallization pressures in the range 359–761 MPa with mean values of 603 ± 94 and 477 ± 77 MPa for Búðahraun and Berserkjahraun, respectively (Fig. 12a and b). Clinopyroxene mantles ($Mg\#_{77-86}$) record different pressures for Búðahraun and Berserkjahraun (Fig. 12c and d): Búðahraun mantles give pressures in the range 197–596 MPa (445 ± 115 MPa), whereas Berserkjahraun mantles record pressures within the range 156–359 MPa (260 ± 59 MPa). Clinopyroxene rims ($Mg\#_{74-83}$) record the lowest overall crystallization pressure range of 110–437 MPa (Fig. 12e and f) with a mean value of 303 ± 78 MPa for Búðahraun. Berserkjahraun rims are compositionally bimodal (Fig. 7a and b) with evolved ($Mg\#_{74-76}$) and primitive ($Mg\#_{79-83}$) populations recording overlapping pressures of 127–373 MPa, with a mean of 261 ± 75 MPa.

Clinopyroxene thermobarometry results are summarized in Fig. 13. For comparison, the five thermally different magmatic environments (coloured areas) for macrocryst cores (C_1 and C_2), mantles (M_3) and rims (R_4 and R_5) are shown. Although erupted from two distinct volcanic systems ∼30 km apart, clinopyroxenes from Búðahraun and Berserkjahraun appear to have formed over a large but similar pressure interval (110–761 MPa), with successive clinopyroxene populations (cores → rims) recording dominant crystallization levels centred around 552 ± 107 and 297 ± 79 MPa. Assuming a mean oceanic crustal density of 2860 kg/m^3 (Carlson & Herrick, 1990), the two main crystallization levels translate to depths of 20 ± 4 and 11 ± 3 km, respectively.

Estimates of the depth to the Moho along the Snæfellsnes peninsula range from ∼20–26 km in the west to ∼25–29 km towards the east (e.g. Darbyshire, 2000; Du *et al.*, 2002; Foulger *et al.*, 2003; Kumar, *et al.*, 2007). In this context, the deep crystallization level located at 20 ± 4 km, mainly recorded by clinopyroxene cores, indicates near-Moho magma storage in the lower crust, whereas the second, much shallower (11 ± 3 km) crystallization level, mainly recorded by the rims, suggests magma storage at upper-mid-crustal levels (Fig. 13). Clinopyroxene mantles display highly variable crystallization depths (6–21 km) overlapping with the cores and the rims.
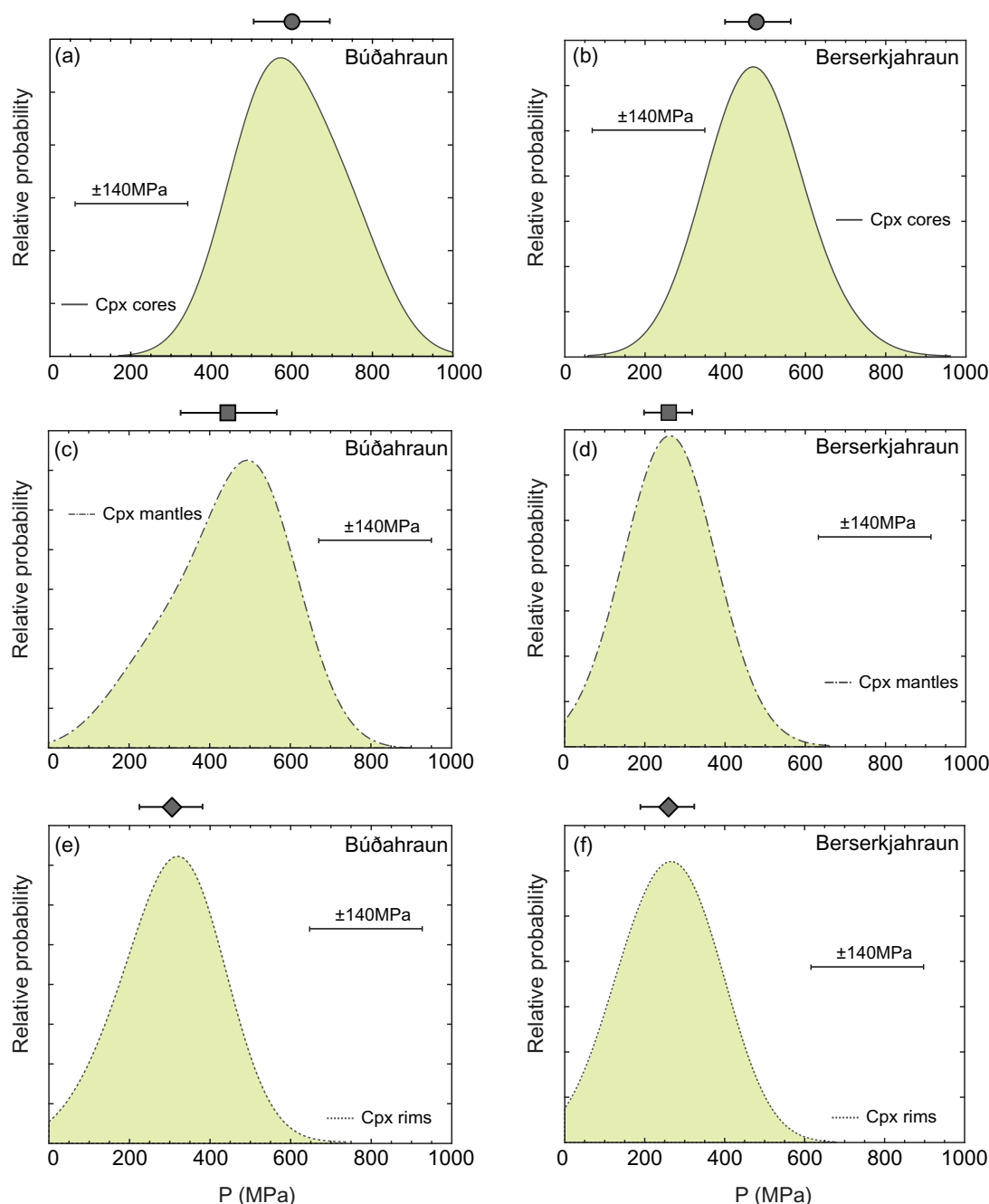
Fig. 12. Kernel density estimates (KDEs) showing pressure distributions for clinopyroxene-liquid pairs from Búðahraun (A, C, E) and Berserkjahraun (B, D, F). Error bars refer to the standard error of estimate (SEE) of the calibrated barometer. KDEs were calculated using a bandwidth of 100 MPa. Grey symbols above each graph show the mean values for each population, black bars refer to 1σ errors.

The thermal record demonstrates that adjacent primitive (antecrystic) and evolved (antecrystic and phenocrystic) core populations formed within two thermally distinct environments, C_1 and C_2 located in the lower crust. The barometric record shows, however, that most core populations, irrespective of primitive or evolved ancestry, have formed within the same pressure interval of 359–761 MPa (552 ± 107 MPa) (Fig. 13). The same applies to primitive and evolved rim populations observed in Berserkjahraun samples. Although

the thermal record suggests formation within two distinct magmatic environments, R_4 and R_5, the pressure record indicates that both rim populations crystallized within the same pressure interval of 110–437 MPa (297 ± 79 MPa). This shows that neighbouring primitive and evolved crystal populations in the Búðahraun and Berserkjahraun crystal cargoes reflect crystal growth and evolution within thermally distinct magmatic environments and do not represent growth at resolvably different depths. Successive crystal populations, in
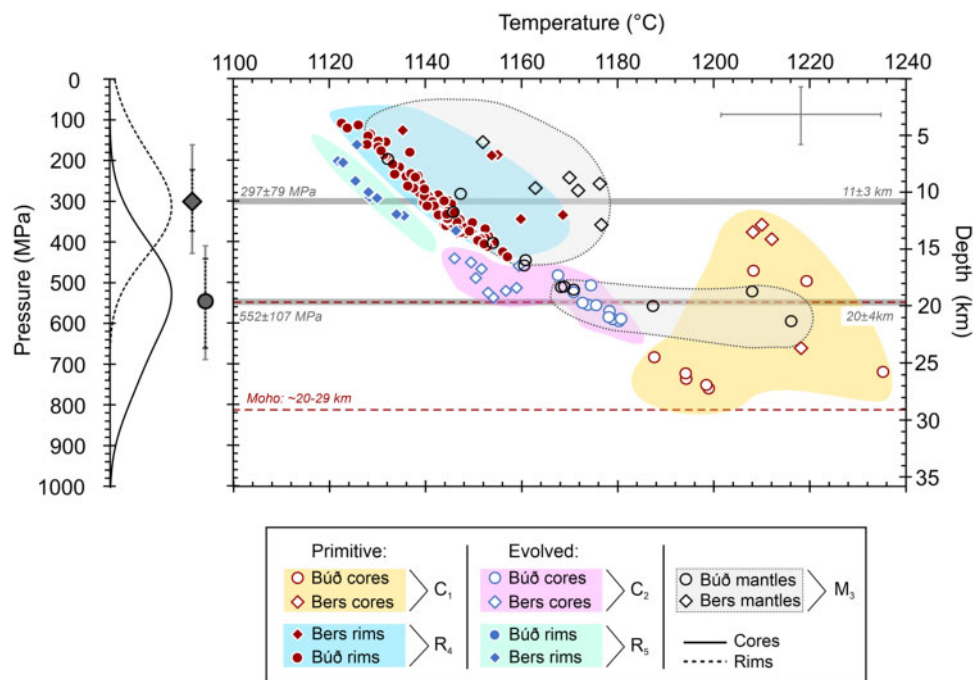
Fig. 13. Clinopyroxene crystallization pressures and depths versus temperature for Búðahraun and Berserkjahraun. Grey horizontal lines highlight the depth range of shallow (11 ± 3 km) and deep (20 ± 4 km) magma storage at Búðahraun and Berserkjahraun. Coloured fields represent the different thermal magmatic environments as identified based on the combined compositional and thermal record of all macrocrysts. C_1 and C_2, primitive and evolved core environments; M_3, transient mixing environment represented by macrocryst mantles. R_4 and R_5, primitive and evolved rim environments. Depth (km) refers to the crust beneath the SNVZ based on a mean oceanic crustal density of 2860 kg/m^3 (Carlson & Herrick, 1990). KDEs depict pressure distributions for core and rim populations from Búðahraun and Berserkjahraun and were calculated using a bandwidth of 100 MPa. Mean pressure values for core and rim populations are shown beside the KDEs. Error bars refer to the standard errors of estimate (SEE) of the clinopyroxene-melt barometer of Neave & Putirka (2017; SEE: ± 140 MPa) and the Jd-DiHd (Jadeite-Diopside Hedenbergite) exchange thermometer of Putirka (2008; SEE: $\pm 45^\circ$C).

contrast, reveal a general decompression trend with cores crystallizing at deeper levels than rims, and mantles being transitional (Fig. 13 and Supplementary Data Table 10).

DISCUSSION

Heterogeneous crystal cargoes: evidence for basaltic cannibalism

Detailed examination of thin sections from lava and scoria from the postglacial Búðahraun and Berserkjahraun eruptions reveals compositionally heterogeneous macrocryst cargoes, with co-existing evolved and primitive macrocryst populations recording distinct evolutionary histories (e.g. Thomson & Maclennan, 2013; Neave et al., 2014, 2015; Hartley et al., 2016; Halldórsson et al., 2018; Pankhurst et al., 2018; Caracciolo et al., 2020). Most macrocryst cores and mantles, but also some rims, represent antecrystic material, either too primitive or too evolved to be in equilibrium with the carrier liquids. The observed thin-section-scale complexity is further enhanced as antecrystic and phenocrystic materials in both localities not only occur in different crystals but are also superimposed on each other on the scale of individual crystals.

Therefore, inter- as well as intra-crystal populations (i.e. cores, mantles and rims) must have experienced different petrogenetic histories in different parts of both magmatic systems (e.g. Cashman & Blundy, 2013). This observation is underpinned by the existence of trace element variability and zoning, not only among clinopyroxenes from both localities but also between successive clinopyroxene zones within individual crystals from the same sample. Primitive clinopyroxene cores are rich in Cr and Ni, and poor in La, Ce, Nd and Zr (Supplementary Data Fig. S1.9), while evolved cores are poor in Cr and Ni, and rich in La, Ce, Nd and Zr (Supplementary Data Figs. S1.8 and S1.10). This confirms that evolved and primitive clinopyroxene cores have formed within compositionally distinct environments. This view is further supported by clinopyroxene equilibrium melt compositions (Fig. 10), which show that melts in equilibrium with primitive and evolved core populations differ in their Yb_N contents by one order of magnitude (0.19–1.89). The same applies to Mg-rich clinopyroxene mantles and rims, which contain Cr-rich zones that are also rich in Ni and Sc (Supplementary Data Fig. S1.10) and poor in La, Nd and Zr (Supplementary Data Fig. S1.8). These Mg-rich mantles and rims have formed from a much narrower range

of melt compositions (Yb$_N$: 0.44–0.70), that plot along the same fractional crystallization trend (Fig. 10). This indicates that although successive clinopyroxene populations crystallized from compositionally and probably also thermally distinct melts (since some of the core and mantle populations display sector zoning), probably in different parts of the plumbing system, they are geochemically related.

But what exactly makes Búðahraun and Berserkjahraun stand out from other well-documented Icelandic eruptions? The first and most obvious aspect is that the compositional diversity of the Búðahraun and Berserkjahraun crystal cargoes is not limited to one macrocryst phase (e.g. clinopyroxene) or a specific intra-crystal population (e.g. cores). Instead, the compositional heterogeneity in Búðahraun and Berserkjahraun encompasses the entire macrocryst record suggesting that all macrocryst phases have experienced similarly complex evolutionary histories. Additionally, the diverse zoning record can be tracked throughout all macrocryst phases. Macrocrysts from Vatnafell (Burney *et al.*, 2020; Fig. 9) and other localities (e.g. Ólafsvíkurenni and Nykurhraun, van der Meer *et al.*, in press) along the SNVZ show predominantly normal zoning. In contrast, Búðahraun and Berserkjahraun macrocryst zoning ranges from simple normal and reverse zoning to complex patterns consisting of reverse-zoned crystal interiors that may be sector zoned, followed by normally zoned outermost rims (Fig. 2). Reverse and complex zoning patterns have been interpreted as indicators for open system processes including magma recharge and magma mixing (Streck, 2008).

Coupled enrichments in the compatible transition metals Cr-Ni-(Sc) and depletions in the incompatible elements La-Nd-Zr along concentric zones have been interpreted as indicators of mafic magma recharge and mixing shortly before eruption (Ubide *et al.*, 2015, 2019*a*; Ubide & Kamber, 2018). This view is further supported by the irregular shapes of corroded, Cr-poor and low-Mg-number clinopyroxene cores. Corroded cores with pervasive resorption features and subrounded, ovoidal shapes are not limited to clinopyroxene but also occur in plagioclase and olivine (Fig. 2; Supplementary Data Figs. S1.1, 1.2 and 1.3). It is likely that corroded primitive and evolved macrocryst cores represent partial resorption on mafic recharge into a compositionally heterogeneous crystal mush. In contrast, clinopyroxenes with oscillatory zoned mantles containing multiple zones of Cr enrichment (Fig. 8p) record repeated magma injections that either failed to trigger eruptions or to evacuate the entire crystal cargo (e.g. Ubide & Kamber, 2018; Ubide *et al.*, 2019*b*).

Overall, we propose that the thin-section-scale complexity observed in the products of the Búðahraun and Berserkjahraun eruptions was caused by repeated recharge events, whereby crystal populations recording evolution within diverse parts of the magmatic systems were entrained and amalgamated into the erupted carrier liquid to produce the complex and heterogeneous crystal cargoes we observe today. This process of

crystal entrainment from different parts of individual sub-volcanic systems via magma recharge and partial digestion (resorption) of entrained crystals has been observed at a variety of arc magmatic systems and is widely known as petrological cannibalism (e.g. Cashman & Blundy, 2013). In Iceland, this process is less well documented, but we believe that basaltic cannibalism (Hudak *et al.*, 2014; LaFemina *et al.*, 2015) could account for much of the textural and compositional heterogeneity observed in Búðahraun and Berserkjahraun.

What distinguishes Búðahraun and Berserkjahraun from other eruptions within the SNVZ (and possibly also from eruptions along the rift zone) is the fact that evidence for basaltic cannibalism in the form of reverse-zoned macrocrysts, resorbed antecrystic cores and compositionally diverse crystal cargoes is well preserved. It thus appears likely that basaltic cannibalism may operate at different lengths and/or timescales within and between different magmatic systems across Iceland.

Conditions and nature of magma storage: on- and off-rift perspectives
Magma storage conditions in on-rift areas
Deep magma storage and processing at lower-crustal levels is not confined to the SNVZ. A prominent and well-studied on-rift example is the early postglacial (10.5–7 ka) Borgarhraun eruption in the Theistareykir system within the Northern Volcanic Zone in Iceland (Maclennan *et al.*, 2001). Combined geothermobarometry, melt inclusion and diffusion chronometry studies have shown that the Borgarhraun magma was stored for nearly 1000 years in a crystalline mush in the lower crust (∼17–24 km) before it was remobilized and transported to the surface in as little as 4 days (Maclennan *et al.*, 2001; Mutch *et al.*, 2019*a*, 2019*b*; Neave & Putirka, 2017; Winpenny & Maclennan, 2011). Despite most evidence for deep magma storage being geophysical (e.g. Tryggvason, 1986; Soosalu & Einarsson, 2004; Sturkell *et al.*, 2006; White *et al.*, 2011; Tarasewicz *et al.*, 2012*a*, 2012*b*; Greenfield *et al.*, 2016; Hudson *et al.*, 2017), most eruptions along the neovolcanic rift-zone record robust petrological evidence for mid-crustal magma storage (e.g. Caracciolo *et al.*, 2020; Hartley *et al.*, 2018; Halldórsson *et al.*, 2018; Neave & Putirka, 2017; Haddadi *et al.*, 2017), which in case of the Bárðarbunga system seems to represent a persisting feature since the last ice age. Older sub-glacial and early Holocene eruptive units within the Bárðarbunga system, however, preserve records of crystallization in the lower crust (∼18 km). The absence of deep crystallization signatures in younger Bárðarbunga eruption units suggests temporal changes in the plumbing structure, including the formation of new magma pathways favouring mid-crustal crystallization conditions (Caracciolo *et al.*, 2020). Multitiered magma storage and evolution in the mid- (9–10 km) and upper- (7–8 km) crust is recorded by

compositionally bimodal clinopyroxene ($Mg\#_{cpx} > 80$; $Mg\#_{cpx} < 80$) core populations (Passmore, 2009; Neave et al., 2013, 2015; Neave & Putirka, 2017). This is, however, different from the off-rift eruptions of Búðahraun and Berserkjahraun, where polybaric magma storage and processing at lower and upper-mid-crustal levels are recorded by successive crystal zones rather than different crystal populations.

Magma storage conditions along the SNVZ and other off-rift areas

Our identification of multi-level magma storage within the SNVZ is consistent with the findings of previous petrological studies in off-rift volcanoes. Burney et al. (2020) demonstrated that magma storage at Vatnafell, a small Upper Pleistocene sub-glacial tuya south of Berserkjahraun (Fig. 1b), occurs over a range of crustal depths. Similar to Búðahraun and Berserkjahraun, Vatnafell also contains bimodal clinopyroxene core compositions (Fig. 9), with evolved cores ($\sim Mg\#_{76}$) occurring in gabbroic glomerocrysts and intermediate cores ($\sim Mg\#_{84}$) featuring predominantly in wehrlitic glomerocrysts. While evolved clinopyroxene cores record pressures and temperatures of 380 ± 40 MPa (14 ± 1 km) and 1162 ± 6°C, primitive cores return much higher crystallization pressures and temperatures of 620 ± 40 MPa (22 ± 1 km) and 1214 ± 5°C. The temperature estimates for the different Vatnafell core populations are consistent with temperatures of 1166 ± 12°C for evolved ($Mg\#_{73-78}$) and 1207 ± 13°C for primitive ($Mg\#_{79-88}$) clinopyroxene core populations obtained for Búðahraun and Berserkjahraun. In contrast with Vatnafell, variably evolved Búðahraun and Berserkjahraun core pressures of 552 ± 107 MPa correspond to slightly shallower crystallization depths of 20 ± 4 km. Vatnafell clinopyroxene rims and groundmass crystals ($\sim Mg\#_{75}$) give pressures of 350 ± 80 MPa (13 ± 3 km) and temperatures of 1152 ± 9°C. This overlaps with the pressure (279 ± 79 MPa; 11 ± 3 km) and temperature (1142 ± 9°C) estimates obtained for Búðahraun and Berserkjahraun clinopyroxene rims ($Mg\#_{74-83}$), with the exception that Berserkjahraun rims are compositionally bimodal requiring the presence of two different magmatic environments.

The overarching view of transcrustal magma storage within the central part of the SNVZ appears to be consistent with magma ponding zones centred in the lower- ($\sim$20–22 km) and upper-mid-crust ($\sim$11–14 km). In fact, the nature and conditions of magma storage are not only spatially but also temporally consistent. That is, the combined petrological record from Búðahraun, Berserkjahraun (<11.5 ka) and Vatnafell ($\sim$410 ka) suggests that the nature and conditions of transcrustal magma storage along the central parts of the SNVZ has remained largely unchanged since the Upper Pleistocene.

Besides the SNVZ, there are two other known off-rift flank zones in Iceland. One of them is the South Iceland

Volcanic Zone (SIVZ) at the tip of the southwards-propagating Eastern Volcanic Zone (e.g. Einarsson, 1991; Einarsson, 2008). Magmatism in this area occurs in three volcanic systems outside the main zones of plate spreading: Eyjafjallajökull, Katla and Vestmannaeyjar (e.g. Nikkola et al., 2019b). A petrologic and geobarometric study of the 2010 eruption of Eyjafjallajökull conducted by Keiding & Sigmarsson (2012) revealed the presence of multiple magma storage regions in the plumbing system. Primitive basaltic tephra, erupted during the initial flank eruptive phase, recorded crystallization pressures corresponding to lower-crustal levels of $\sim$16–18 km. Highly differentiated benmoreitic tephra that was erupted during the second, explosive summit eruptive phase was found to have crystallized from shallower magma storage at upper crustal levels of $\sim$2–5 km. Intricate and multi-tiered magma plumbing configurations have also been suggested by detailed geophysical and geochemical observations during the eruption (e.g. Sigmundsson et al., 2010; Sigmarsson et al., 2011; Tarasewicz et al., 2012a, 2012b). Interestingly, geothermobarometry applied to older ($\sim$500–720 ka) ankaramitic eruptive units from Eyjafjallajökull located at Brattaskjól and Hvammsmúli shows no signs of polybaric magma storage. Instead, clinopyroxene crystallization indicates mid-crustal magma storage at a depth of $\sim$11 km (Nikkola et al., 2019b).

Contrary to this, a study by Budd et al. (2016) investigating a suite of Katla tephras ranging from 8 ka to 1918 AD observed a multi-tiered plumbing configuration with simultaneous deep to mid-crustal ($\sim$10–25 km) and shallow ($\leq$8 km) magma storage. Recent eruptions from Vestmannaeyjar (Eldfell 1973 AD; Surtsey 1963–67 AD), located at the tip of the southward propagating rift, also indicate that magma processing and evolution have occurred in the lower crust ($\sim$18–20 km) and the upper mantle ($\sim$30–35 km; Furman et al., 1991). In summary, it appears that in contrast with the SNVZ, not only magma storage but also plumbing geometries have varied since the Upper Pleistocene in the SIVZ, with deeper magma storage becoming more prominent in recent times.

In the context of these observations, a general view of polybaric magma storage within dynamically changing multi-tiered off- and on-rift magmatic systems across Iceland emerges (e.g. Maclennan, 2019). Furthermore, off-rift eruption products often preserve evidence for late-stage mafic recharge events in the form of widespread reverse and complex zoning of macrocryst phases (e.g. Pankhurst et al., 2018; Nikkola et al., 2019b; Sigmarsson et al., 2011; this study; Keiding & Sigmarsson, 2012). On-rift eruptions by contrast do not preserve direct evidence for late-stage, eruption-triggering mafic recharge events (e.g. Hartley et al., 2016; Caracciolo et al., 2021). We therefore propose that on- and off-rift eruptions differ in their eruption-triggering mechanisms. Eruptions along the main rift zones may be triggered by tectonic processes (e.g.

Caracciolo *et al.*, 2021), whereas off-rift eruptions often preserve evidence for recharge-related eruption triggering.

Reconstruction of the plumbing system feeding Búðahraun and Berserkjahraun

One of the key factors controlling the depths of magma storage levels at oceanic intraplate volcanoes is the magma supply rate, which has a strong control on the thermomechanical properties of the lithosphere (e.g. Stroncik *et al.*, 2009). At high magma supply rates, the heat flux of the lithosphere may become sufficiently high to favour the establishment of a long-lived shallow magma chamber (e.g. Clague & Dixon, 2000), whereas low magma supply rates favour freezing of early produced melts and fractionation until a stable plumbing system has been established (e.g. Devey *et al.*, 2003; Klügel & Klein, 2006). Indeed, the presence or absence

of shallow magma chambers is thought to play an important role in controlling differences in the chemistry and mineralogy of mid-ocean ridge basalts erupted on-axis and from off-axis seamounts, respectively (Sours-Page *et al.*, 2002). In Iceland, geothermal gradients and melt productions rates decrease with increasing distance from the rift zones and the plume centre (e.g. Sigurdsson, 1970; Flóvenz & Sæmundsson, 1993; Martin & Sigmarsson, 2007; Sigmarsson *et al.*, 2008). Hence, off-rift volcanic zones are usually characterized by much lower geothermal gradients and melt production rates. The reduced heat flow within the SNVZ could explain the diversity of the Búðahraun and Berserkjahraun crystal cargoes. In particular, the occurrence of highly evolved plagioclase and clinopyroxene core compositions (Fig. 9) suggest that evolved melts existed in both plumbing systems. This is in agreement with the occurrence of highly fractionated silicic magmas along the SNVZ, which are attributed to the colder

Fig. 14

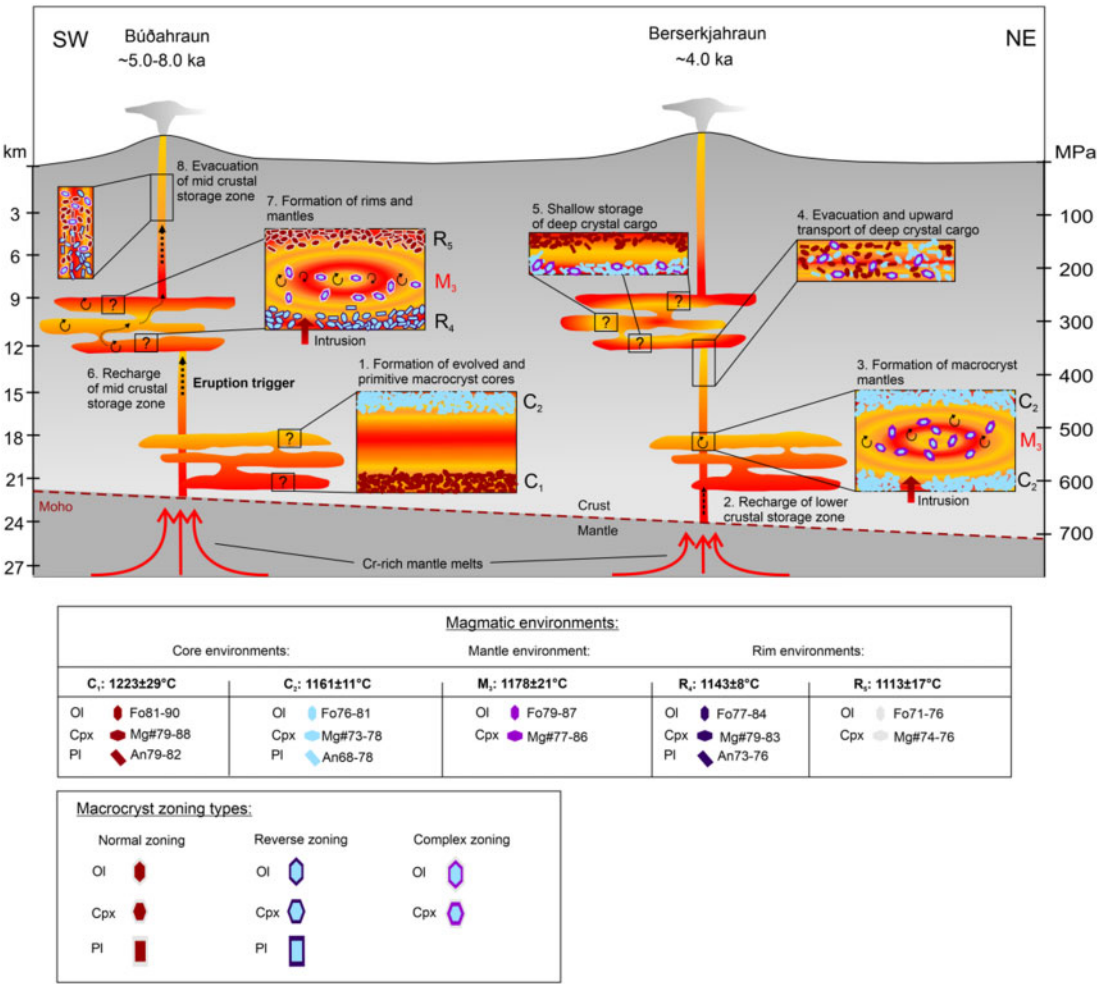**Fig. 14.** Schematic model summarizing the conditions and dynamics of magma storage and transfer within the sub-volcanic magmatic systems underneath Búðahraun and Berserkjahraun. Question marks refer to the depth limitations of our model, associated with the standard error of estimate (SEE: ±140 MPa) of the applied clinopyroxene-liquid barometer (Neave & Putirka, 2017 and Neave *et al.*, 2019).

thermal state of the crust (e.g. Martin & Sigmarsson, 2007).

Heterogeneous crystal cargoes with crystal populations more evolved than the carrier liquids are also reported from ocean island volcanoes in Galápagos (e.g. Wolf and Fernandina; Stock *et al.*, 2020) and the Canary Islands (e.g. El Hierro, Stroncik *et al.*, 2009; La Palma, Klügel *et al.*, 2000). Similar to Icelandic off-rift zones, the Canary Islands are characterized by low magma supply rates. Hence, periodic mixing between primitive and evolved batches of melt is considered to occur within a network of partly interconnected ephemeral melt pockets (e.g. Klügel *et al.*, 2005; Stroncik *et al.*, 2009; Klügel *et al.*, 2015). The concept of multiple, partly interconnected melt pockets, each with its own distinctive compositional evolution, could explain the compositional and textural zoning diversity of the Búðahraun and Berserkjahraun crystal cargoes.

In this context, we propose a conceptual model of transcrustal magma transfer, storage and mixing, as summarized in Fig. 14. Primitive and evolved macrocryst cores formed within two compositionally and thermally distinct magmatic environments, C_1 and C_2, located within the lower crust (stage 1). The formation of macrocryst mantles was associated with the magmatic environment M_3, which overlaps with the two core environments C_1 and C_2 and the primitive rim environment R_4 (Fig. 13). Linking clinopyroxene trace element data with the thermometric record demonstrates that Mg-, Ni- and Cr-rich mantles formed upon the arrival of a hotter ($\sim$1180°C) and more primitive melt. Overlapping of the mantle environment M_3 with the core and rim environments reflects the arrival of batches of mafic melt into different segments of the system. We conclude that early injections of primitive melt into the deep storage zone (stage 2) caused the formation of the transient mixing environment M_3, followed by the subsequent formation of primitive mantles enclosing evolved olivine and clinopyroxene cores (stage 3). Periodic flushing of the lower-crustal storage zone with primitive basaltic magma weakens the dense mush fabric, resulting in the entrainment, upward transport and storage of the compositionally heterogeneous deep crystal cargo at mid-crustal levels (stages 4 and 5). Injections of mafic melt into the mid-crustal storage zone causes widespread mixing with evolved ancestral melts resulting in the formation of the transient mixing environment M_3 and the primitive rim environment R_4, giving rise to the formation of Mg- and Cr- (Ni- and ±Sc-) rich macrocryst mantles and rims (Stage 6 and 7). Progressive mixing with evolved melts possibly led to the formation of a second rim environment R_5 in which the more evolved macrocrysts' rims have formed. As evidenced by the occurrence of Cr-enriched ($>10^3$ppm) clinopyroxene mantles and rims, recharge of the shallow mid-crustal storage zone was powerful enough to tip over the system to erupt, resulting in the amalgamation of crystals with different ancestries from diverse parts of the subvolcanic systems (stage 8). Dynamic crystallization regimes on recharge, mixing and magma ascent are reflected in the development of sector zoning in the mantle and core zones of the clinopyroxene crystals.

Implications for volcano monitoring

Similar complex eruption and magma plumbing dynamics have been reported from other Icelandic off-rift eruptions. The most prominent examples are the closely monitored 2010 flank (20 March to 12 April) and summit (14 April to late May) eruptions of Eyjafjallajökull within the SIVZ. Preceded by 18 years of intermittent unrest, volcanic activity culminated in the onset of a flank eruption on March 20, followed by two explosive summit eruptive phases (Sigmundsson *et al.*, 2010). After the initiation of summit eruptive activity on 14 April, triggered by mafic melt recharging an evolved silicic shallow reservoir ($\sim$5 km) beneath the summit crater, explosive activity gradually changed into effusive lava eruptions (e.g. Sigmarsson *et al.*, 2011). Detailed observations of the 2010 Eyjafjallajökull summit eruptions show vertically propagating seismic activity during a ten-week period consisting of several explosive episodes. Systematic changes in magma chemistry suggest intricate magma plumbing dynamics with tapping of sills at different crustal levels and distinctive compositional evolution. During the eruption, a systematic downward propagation of seismic activity throughout the crust and into the uppermost mantle occurred in a series of steps, each of which preceded an explosive eruptive event by 1–3 days (e.g. Tarasewicz *et al.*, 2012b). The sequence of seismicity and eruptive activity was best explained by the downward propagation of a decompression wave caused by the progressive depressurization of the shallow summit reservoir, which triggered magma release from progressively deeper melt reservoirs in the crust (e.g. Tarasewicz *et al.*, 2012b; Sigmarsson *et al.*, 2011).

Transferring an eruption scenario like this to the poorly monitored SNVZ suggests that while the reawakening of volcanic activity along the SNVZ could be preceded by years of subtle volcanic unrest (e.g. inflation signals), the fast remobilization of large volumes of magma from lower to upper crustal levels via basaltic flushing of different magma storage zones and the successive destabilization of melt lenses may occur on short timescales on the order of a few days, providing little warning for emergency planning. Due to the insufficient monitoring status of the SNVZ short- to immediate-term precursor activity could be difficult to detect due to the general lack of long-term monitoring (e.g. Jóhannesson, 2019). A further intricacy is that the Holocene eruptions of Búðahraun and Berserkjahraun comprise evidence for recharge-induced eruption triggering. This is even more critical as highly fractionated silicic magmas are found in all three volcanic systems (Snæfellsjökull, Lýsuskarð and Ljósufjöll) of the SNVZ, increasing the likelihood for potentially hazardous explosive eruptions, such as the 2010 eruptions of Eyjafjallajökull, triggered by intrusions of mafic magma

into highly evolved silicic melt pockets. In fact, the latest explosive Plinian eruption (SN-1) of Snæfellsjökull, in the west of the SNVZ, occurred at 1750 BP (Steinthórsson *et al.*, 1967).

Given the limited petrological record and poor monitoring status of the SNVZ, insights gained from the diverse macrocryst cargoes of Búðahraun and Berserkjahraun provide essential information for the development of future monitoring efforts and for the assessment of hazards along the Snæfellsnes peninsula. Although volcanism within the SNVZ differs fundamentally from the rift zones with eruptions not being controlled by extensional spreading, magma ascent from depth still appears to follow pre-existing tectonic escape routes and may occur within a few days' notice. The vital next stage to advise future monitoring efforts is to obtain a more detailed view on the critical timescales and durations of magma residence and magma transfer within the SNVZ.

CONCLUSIONS

We have presented a combined geochemical and geothermobarometric study of conditions and dynamics of magma storage and magma transfer recorded in the products of the postglacial Búðahraun ($\sim$5.0–8.0 ka) and Berserkjahraun ($\sim$4.0 ka) eruptions within the SNVZ, one of Iceland's largest regions of off-rift volcanism. Our main findings are as follows:

1. Detailed petrologic examination unveils intricate plumbing system dynamics for the Holocene eruptions of Búðahraun and Berserkjahraun, which reflect the transfer and amalgamation of crystals with distinct ancestries from different parts of the subvolcanic systems. Compositional and textural diversity are directly linked to the thermal state of the crust and hence its position relative to the mantle plume centre and the lack of extension. We invoke a petrogenetic model whereby low heat flow underneath the SNVZ favours cooling and fractionation of early produced melts resulting in the formation of partly interconnected melt pockets, each with their own compositional and temporal evolution. Periodic flushes of primitive basaltic magma from depths promote widespread mixing with evolved melts, resulting in the assembly of crystals with different ancestries. This is similar to other intraplate volcanoes with low magma supply rate.
2. Combined macrocryst and melt inclusion variability requires the presence of compositionally diverse parental melts in both plumbing systems. Initial compositional variability is not preserved with melt evolution, as emphasized by the eruption of less variable carrier liquid compositions.
3. Mineral-melt thermometry enables identification of distinct magmatic environments in which adjacent and successive crystal populations evolved. The compositional bimodality of macrocryst cores, rims and ±mantles with evolved and primitive populations enables the identification of five thermally distinct magmatic environments: C_1 [1223 ± 29°C], C_2 [1161 ± 11°C] (cores), M_3 [1178 ± 21°C] (mantles), R_4 [1143 ± 8°C] and R_5 [1113 ± 17°C] (rims).
4. Successive clinopyroxene populations from Búðahraun and Berserkjahraun reveal the existence of two dominant crystallization levels with pressures around 552 ± 107 (cores) and 297 ± 79 MPa (rims), corresponding to depths of 20 ± 4 and 11 ± 3 km, consistent with the existence of two thermally and compositionally heterogeneous magma storage regions located at lower- and upper-mid-crustal levels. Crystallization pressure and depth estimates coincide with clinopyroxene-melt barometry data from Vatnafell, suggesting that the nature and conditions of magma storage within the central parts of the SNVZ have remained unchanged since the Upper Pleistocene.
5. Textural and compositional indicators for eruption-triggering recharge and basaltic cannibalism are ubiquitous and well preserved, setting the Búðahraun and Berserkjahraun eruptions apart from on-rift eruptions in Iceland. Geothermobarometric records combined with trace element mapping enables reconstruction of the arrival of batches of mafic melt into different parts of both plumbing systems. Mafic intrusions into the mid-crustal storage zone shortly before eruption highlight how magma recharge triggered the eruptions of Búðahraun and Berserkjahraun. This behaviour is similar to other off-rift eruptions in Iceland (e.g. 2010 Eyjafjallajökull). Records of recurrent recharge preserved as Cr-rich zones in oscillatory zoned clinopyroxene mantles may have been less effective in triggering eruptions, but provide a snapshot of events that primed the plumbing systems for eruption.

SUPPLEMENTARY DATA

Supplementary data are available at *Journal of Petrology* online.

REFERENCES

Budd, D. A., Troll, V. R., Dahren, B. & Burchardt, S. (2016). Persistent multitiered magma plumbing beneath Katla volcano. *Geochemistry, Geophysics, Geosystems* **17**, 966–980. doi:10.1002/2015GC006118

Burney, D., Peate, D. W., Riishuus, M. S. & Ukstins, I. A. (2020). Reconstructing the plumbing system of an off-rift primitive alkaline tuya (Vatnafell, Iceland) using geothermobarometry and CSDs. *Journal of Volcanology and Geothermal Research* **399**, 106914. doi:10.1016/j.jvolgeores.2020.106914

Caracciolo, A., Bali, E., Guðfinnsson, G. H., Kahl, M., Halldórsson, S. A., Hartley, M. E. & Gunnarsson, H. (2020). Temporal evolution of magma and crystal mush storage conditions in the Bárðarbunga-Veiðivötn volcanic system, Iceland. *Lithos* **352-353**, 105234. doi:10.1016/j.lithos.2019.105234

Caracciolo, A., Kahl, M., Bali, E., Guðfinnsson, G. H., Halldórsson, S. A. & Hartley, M. E. (2021). Timescales of crystal mush mobilization in the Bárðarbunga-Veiðivötn volcanic system based on olivine diffusion chronometry. *American Mineralogist* **106** (7), 1083–1096. doi:10.2138/am-2021-7670

Carlson, R. & Herrick, C. (1990). Densities and porosities in the oceanic crust and their variations with depth and age. *Journal of Geophysical Research* **95**, 9153–9170. doi:10.1029/JB095iB06p09153

Cashman, K. V. & Blundy, J. D. (2013). Petrological cannibalism: the chemical and textural consequences of incremental magma body growth. *Contributions to Mineralogy and Petrology* **166**, 703–729. doi:10.1007/s00410-013-0895-0

Cashman, K. V., Sparks, R. S. J. & Blundy, J. D. (2017). Vertically extensive and unstable magmatic systems: a unified view of igneous processes. *Science* **355**, eaag3055. doi:10.1126/science.aag3055

Clague, D. A. & Dixon, J. E. (2000). Extrinsic controls on the evolution of Hawaiian ocean island volcanoes. *Geochemistry, Geophysics, Geosystems* **1**, 1010. doi:10.1029/1999GC000023

Darbyshire, F. A., White, R. S. & Priestley, K. F. (2000). Structure of the crust and uppermost mantle of Iceland from a combined seismic and gravity study. *Earth and Planetary Science Letters* **181**, 409–428. doi:10.1016/S0012-821X(00)00206-5

Davidson, J. P., Morgan, D. J., Charlier, B. L. A., Harlou, R. & Hora, J. R. (2007). Microsampling and isotopic analysis of igneous rocks: implications for the study of magmatic systems. *Annual Review of Earth and Planetary Sciences* **35**, 273–311. doi:10.1146/annurev.earth.35.031306.140211

Debaille, V., Trønnes, R. G., Brandon, A. D., Waight, T. E., Graham, D. W. & Lee, C.-T. (2009). Primitive off-rift basalts from Iceland and Jan Mayen: Os-isotopic evidence for a mantle source containing enriched subcontinental lithosphere. *Geochimica et Cosmochimica Acta* **73**, 3423–3449. doi:10.1016/j.gca.2009.03.002

Devey, C. W., Lackschewitz, K. S., Mertz, D. F., Bourdon, B., Cheminée, J. L., Dubois, J., Guivel, C., Hékinian, R. & Stoffers, P. (2003). Giving birth to hotspot volcanoes: Distribution and composition of young seamounts from the seafloor near Tahiti and Pitcairn islands. *Geology* **31**, 395–398. doi:10.1130/0091-7613(2003)031<0395:GBTHVD>2.0.CO;2

Du, Z., Foulger, G. R., Julian, B. R., Allen, R. M., Nolet, G., Morgan, W. J., Bergsson, B. H., Erlendsson, P., Jakobsdottir, S., Ragnarsson, S., Stefansson, R. & Vogfjord, K. (2002). Crustal structure beneath western and eastern Iceland from surface waves and receiver functions. *Geophysical Journal International* **149**, 349–363. doi:10.1046/j.1365-246X.2002.01642.x

Edmonds, M., Cashman, K. V., Holness, M. & Jackson, M. (2019). Architecture and dynamics of magma reservoirs. *Philosophical Transactions of the Royal Society A* **377**, 1–29. doi:10.1098/rsta.2018.0298

Einarsson, P. (1991). Earthquakes and present-day tectonism in Iceland. *Tectonophysics* **189**, 261–279. doi:10.1016/0040-1951(91)90501-I

Einarsson, P. (2008). Plate boundaries, rifts and transform faults in Iceland. *Jökull* **58**, 35–59.

Flóvenz, Ó. G. & Saemundsson, K. (1993). Heat flow and geothermal processes in Iceland. *Tectonophysics* **225**, 123–138. doi:10.1016/0040-1951(93)90253-G

Flude, S., Burgess, R. & McGarvie, D. W. (2008). Silicic volcanism at Ljósufjöll, Iceland: insights into evolution and eruptive history from Ar–Ar dating. *Journal of Volcanology and Geothermal Research* **169**, 154–175. doi:10.1016/j.jvolgeores.2007.08.019

Foulger, G. R., Du, Z. & Julian, B. R. (2003). Icelandic-type crust. *Geophysical Journal International* **155**, 567–590. doi:10.1046/j.1365-246X.2003.02056.x

Furman, T., Frey, F. A. & Park, K.-H. (1991). Chemical constraints on the petrogenesis of mildly alkaline lavas from Vestmannaeyjar, Iceland: the Eldfell (1973) and Surtsey (1963-1967) eruptions. *Contributions to Mineralogy and Petrology* **109**, 19–37. doi:10.1007/BF00687198

Greenfield, T., White, R. S. & Roecker, S. (2016). The magmatic plumbing system of the Askja central volcano, Iceland, as imaged by seismic tomography. *Journal of Geophysical Research: Solid Earth* **121**, 7211–7229. doi:10.1002/2016JB013163

Gudmundsson, A. (2000). Dynamics of volcanic systems in Iceland: example of tectonism and volcanism at juxtaposed hot spot and mid-ocean. *Annual Review of Earth and Planetary Sciences* **28**, 107–140. doi:10.1146/annurev.earth.28.1.107

Gudmundsson, A. (2007). Infrastructure and evolution of ocean-ridge discontinuities in Iceland. *Journal of Geodynamics* **43**, 6–29. doi:10.1016/j.jog.2006.09.002

Haddadi, B., Sigmarsson, O. & Larsen, G. (2017). Magma storage beneath Grímsvötn volcano, Iceland, constrained by clinopyroxene-melt thermobarometry and volatiles in melt inclusions and groundmass glass. *Journal of Geophysical Research: Solid Earth* **122**, 6984–6997. doi:10.1002/2017JB014067

Halldórsson, S. A., Bali, E., Hartley, M. E., Neave, D. A., Peate, D. W., Guðfinnsson, G. H., Bindeman, I., Whitehouse, M. J., Riishuus, M. S., Pedersen, G. B. M., Jakobsson, S., Askew, R., Gallagher, C. R., Guðmundsdóttir, E. R., Gudnason, J., Moreland, W. M., Oskarsson, B. V., Nikkola, P., Reynolds, H. I., Schmith, J. & Thordarson, T. (2018). Petrology and geochemistry of the 2014–2015 Holuhraun eruption, central Iceland: compositional and mineralogical characteristics, temporal variability and magma storage. *Contributions to Mineralogy and Petrology* **173**, 64. doi:10.1007/s00410-018-1487-9

Hansen, H. & Grönvold, K. (2000). Plagioclase ultraphyric basalts in Iceland: the mush of the rift. *Journal of Volcanology and Geothermal Research* **98**, 1–32. doi:10.1016/S0377-0273(99)00189-4

Harðarson, B. S. (1993). Alkalic rocks in Iceland with special reference to the Snæfellsjökull volcanic system. Unpublished Ph.D. thesis, University of Edinburgh.

Harðarson, B. S. & Fitton, J. G. (1991). Increased mantle melting beneath Snaefellsjökull volcano during Late Pleistocene deglaciation. *Nature* **353**, 62–64. doi:10.1038/353062a0

Harðarson, B. S., Fitton, J. G. & Hjártarson, Á. (2008). Tertiary volcanism in Iceland. *Jökull* **58**, 161–179.

Hart, S. R., Blusztajn, J., Dick, H. J. B., Meyer, P. S. & Muehlenbachs, K. (1999). The fingerprint of seawater circulation in a 500-meter section of ocean crust gabbros. *Geochimica et Cosmochimica Acta* **63**, 4059–4080. doi:10.1016/S0016-7037(99)00309-9

Hartley, M. E., Bali, E., Maclennan, J., Neave, D. A. & Halldórsson, S. A. (2018). Melt inclusion constraints on petrogenesis of the 2014–2015 Holuhraun eruption, Iceland. *Contributions to Mineralogy and Petrology* **173**, 10.doi:10.1007/s00410-017-1435-0

Hartley, M. E., Morgan, D. J., Maclennan, J., Edmonds, M. & Thordarson, T. (2016). Tracking timescales of short-term precursors to large basaltic fissure eruptions through Fe–Mg diffusion in olivine. *Earth and Planetary Science Letters* **439**, 58–70. doi:10.1016/j.epsl.2016.01.018

Hudak, M. R., Feineman, M. D., LaFemina, P. C. & Geirsson, H. (2014). Basaltic cannibalism at Thrihnukagigur volcano, Iceland. *American Geophysical Union, Fall Meeting 2014* abstract id. V43A–4856.2014AGUFM.V43A4856H.

Hudson, T. S., White, R. S., Greenfield, T., Ágústsdóttir, T., Brisbourne, A. & Green, R. G. (2017). Deep crustal melt plumbing of Bárðarbunga volcano, Iceland. *Geophysical Research Letters* **44**, 8785–8794. doi:10.1002/2017GL074749

Jakobsson, S. P. (1972). Chemistry and distribution pattern of recent basaltic rocks in Iceland. *Lithos* **5**, 365–386. doi.org/10.1016/0024-4937(72)90090-4

Janebo, M. H., Thordarson, T., Houghton, B. F., Bonadonna, C., Larsen, G. & Carey, R. J. (2016). Dispersal of key subplinian–Plinian tephras from Hekla volcano, Iceland: implications for eruption source parameters. *Bulletin of Volcanology* **78**, 66.doi:10.1007/s00445-016-1059-7

Jarosewich, E. (2002). Smithsonian microbeam standards. *Journal of Research of the National Institute of Standards and Technology* **107**, 681–685. doi:10.6028/jres.107.054

Jóhannesson, H. (1980). Evolution of rift zones in western Iceland. *Natturufrædingurinn* **50**, 13–31.

Jóhannesson, H. (1982). Yfirlit um jardfraedi Snaefellsness (On the geology of the Snaefellsnes Peninsula, in Icelandic). *Árbok Férdafelags Islands* **1982**, 151–172.

Jóhannesson, H. (2019). Ljósufjöll. In: Oladottir, B., Larsen, G. & Guðmundsson, M. T. Catalogue of Icelandic Volcanoes. IMO, UI and CPD-NCIP. http://icelandicvolcanoes.is/?volcano=KAT

Jóhannesson, H., Flores, M. R. & Jónson, J. (1981). A short account of the Holocene tephrochronology of the Snaefellsjökull central volcano, western Iceland. *Jökull* **31**, 23–30.

Kahl, M., Chakraborty, S., Costa, F. & Pompilio, M. (2011). Dynamic plumbing system beneath volcanoes revealed by kinetic modeling, and the connection to monitoring data: an example from Mt. Etna. *Earth and Planetary Science Letters* **308**, 11–22. doi:10.1016/j.epsl.2011.05.008

Kahl, M., Chakraborty, S., Pompilio, M. & Costa, F. (2015). Constraints on the nature and evolution of the magma plumbing system of Mt. Etna volcano (1991–2008) from a combined thermo- dynamic and kinetic modelling of the compositional record of minerals. *Journal of Petrology* **56**, 2025–2068. doi:10.1093/petrology/egv063

Kahl, M., Viccaro, M., Ubide, T., Morgan, D. J. & Dingwell, D. B. (2017). A branched magma feeder system during the 1669 Eruption of Mt Etna: evidence from a time-integrated study of zoned olivine phenocryst populations. *Journal of Petrology* **58**, 443–472. doi:10.1093/petrology/egx022

Keiding, J. K. & Sigmarsson, O. (2012). Geothermobarometry of the 2010 Eyjafjallajökull eruption: new constraints on Icelandic magma plumbing systems. *Journal of Geophysical Research: Solid Earth* **117**, B00C09. doi:10.1029/2011JB008829

Kinzler, R. J. & Grove, T. L. (1992). Primary magmas of mid-ocean ridge basalts 1. Experiments and methods. *Journal of Geophysical Research* **97**, 6885. doi:10.1029/91JB02840

Klügel, A., Hansteen, T. H. & Galipp, K. (2005). Magma storage and underplating beneath Cumbre Vieja volcano, La Palma (Canary Islands). *Earth and Planetary Science Letters* **236**, 211–226.doi:10.1016/j.epsl.2005.04.006

Klügel, A., Hoernle, K. A., Schmincke, H.-U. & White, J. D. L. (2000). The chemically zoned 1949 eruption on La Palma (Canary Islands): petrologic evolution and magma supply dynamics of a rift-zone eruption. *Journal of Geophysical Research: Solid Earth* **105**, 5997–6016. doi:10.1029/1999JB900334

Klügel, A. & Klein, F. (2006). Complex magma storage and ascent at embryonic submarine volcanoes from the Madeira Archipelago. *Geology* **34**, 337–340. doi:10.1130/G22077.1

Klügel, A., Longpré, M.-A., García-Cañada, L. & Stix, J. (2015). Deep intrusions, lateral magma transport and related uplift at ocean island volcanoes. *Earth and Planetary Science Letters* **431**, 140–149.doi:10.1016/j.epsl.2015.09.031

Kokfelt, T. F., Hoernle, K., Hauff, F., Fiebig, J., Werner, R. & Garbe-Schönberg, D. (2006). Combined trace element and Pb-Nd-Sr-O isotope evidence for recycled oceanic crust (upper and lower) in the Iceland mantle plume. *Journal of Petrology* **47**, 1705–1749. doi:10.1093/petrology/egl025

Kokfelt, T. F., Hoernle, K., Lundstrom, C., Hauff, F. & van den Bogaard, C. (2009). Time-scales for magmatic differentiation at the Snaefellsjökull central volcano, western Iceland: constraints from U–Th–Pa–Ra disequilibria in post-glacial lavas. *Geochimica et Cosmochimica Acta* **73**, 1120–1144.

Kumar, P., Kind, R., Priestley, K. & Dahl-Jensen, T. (2007). Crustal structure of Iceland and Greenland from receiver function studies. *Journal of Geophysical Research* **112**, B03301.doi:10.1029/2005JB003991

LaFemina, P. C., Hudak, M. R., Feineman, M. D., Geirsson, H., Normandeau, J. & Furman, T. (2015). *EGU General Assembly 2015*, held 12–17 April, 2015 in Vienna, Austria. id.9498.

Larsen, G. & Thorarinsson, S. (1977). H4 and other acidic Hekla tephra layers. *Jökull* **27**, 28–46.

Leung, I. S. (1974). Sector-zoned titanaugites: morphology, crystal chemistry, and growth. *American Mineralogist* **59**, 127–138.

Linde, A. T. & Sacks, I. S. (1998). Triggering of volcanic eruptions. *Nature* **395**, 888–890. doi:10.1038/27650

Maclennan, J. (2019). Mafic tiers and transient mushes: evidence from Iceland. *Philosophical Transactions of the Royal Society A: Mathematical, Physical and Engineering Sciences* **377**, 20180021. doi:10.1098/rsta.2018.0021

Maclennan, J., McKenzie, D., Grönvold, K. & Slater, L. (2001). Crustal accretion under northern Iceland. *Earth and Planetary Science Letters* **194**, 67–82. doi:10.1016/S0012-821X(01)00420-4

Magee, R., Ubide, T. & Kahl, M. (2020). The lead-up to Mount Etna's most destructive historic eruption (1669). Cryptic recharge recorded in clinopyroxene. *Journal of Petrology* **61**. doi:10.1093/petrology/egaa025

Martin, E. & Sigmarsson, O. (2007). Crustal thermal state and origin of silicic magma in Iceland: the case of Torfajökull,

Ljósufjöll and Snæfellsjökull volcanoes. *Contributions to Mineralogy and Petrology* **153**, 593–605. doi:10.1007/s00410-006-0165-5

Matthews, S. W. (2019). Deep Earth volatile cycles as revealed by basalt chemistry. Ph.D. thesis. University of Cambridge. doi:10.17863/CAM.40015.

Mollo, S., Putirka, K. D., Misiti, V., Soligo, M. & Scarlato, P. (2013). A new test for equilibrium based on clinopyroxene-melt pairs: clues on the solidification temperatures of Etnean alkaline melts at post-eruptive conditions. *Chemical Geology* **352**, 92–100. doi:10.1016/j.chemgeo.2013.05.026

Mutch, E. J. F., Maclennan, J., Holland, T. J. B. & Buisman, I. (2019b). Millennial storage of near-Moho magma. *Science (New York, NY)* **365**, 260–264. doi:10.1126/science.aax4092

Mutch, E. J. F., Maclennan, J., Shorttle, O., Edmonds, M. & Rudge, J. (2019a). Rapid transcrustal magma movement under Iceland. *Nature Geoscience* **12**, 569–574. doi:10.1038/s41561-019-0376-9

Namur, O., Charlier, B., Toplis, M. J. & Van der Auwera, J. (2012). Prediction of plagioclase-melt equilibria in anhydrous silicate melts at 1-atm. *Contributions to Mineralogy and Petrology* **163**, 133–150. doi:10.1007/s00410-011-0662-z

Neave, D. A., Bali, E., Guðfinnsson, G. H., Halldórsson, S. A., Kahl, M., Schmidt, A.-S. & Holtz, F. (2019). Clinopyroxene–liquid equilibria and geothermobarometry in natural and experimental tholeiites: the 2014–2015 Holuhraun Eruption, Iceland. *Journal of Petrology* **60**, 1653–1680. doi:10.1093/petrology/egz042

Neave, D. A., Maclennan, J., Hartley, M. E., Edmonds, M. & Thordarson, T. (2014). Crystal storage and transfer in basaltic systems: the Skuggafjöll eruption, Iceland. *Journal of Petrology* **55**, 2311–2346.doi:10.1093/petrology/egu058

Neave, D. A., Maclennan, J., Thordarson, T. & Hartley, M. E. (2015). The evolution and storage of primitive melts in the Eastern Volcanic Zone of Iceland: the 10 ka Grímsvötn tephra series (i.e. the Saksunarvatn ash). *Contributions to Mineralogy and Petrology* **170**, 21.doi:10.1007/s00410-015-1170-3

Neave, D. A., Passmore, E., Maclennan, J., Fitton, G. & Thordarson, T. (2013). Crystal-melt relationships and the record of deep mixing and crystallization in the AD 1783 Lakí eruption, Iceland. *Journal of Petrology* **54**, 1661–1690. doi:10.1093/petrology/egt027

Neave, D. A. & Putirka, K. D. (2017). Clinopyroxene-liquid barometry revisited: magma storage pressures under Icelandic rift zones. *American Mineralogist* **102**, 777–794. doi:10.2138/am-2017-5968

Nikkola, P., Bali, E., Kahl, M., van der Meer, Q. H. A., Rämö, O. T., Guðfinnsson, G. H. & Thordarson, T. (2019b). Mid-crustal storage and crystallization of Eyjafjallajökull ankaramites, South Iceland. *Jökull* **69**, 77–96.

Nikkola, P., Guðfinnsson, G. H., Bali, E., Rämö, O. T., Fusswinkel, T. & Thordarson, T. (2019a). Signature of deep mantle melting in South Iceland olivine. *Contributions to Mineralogy and Petrology* **174**, 1–19.doi:10.1007/s00410-019-1580-8

Óskarsson, N., Steinthorsson, S. & Sigvaldason, G. E. (1985). Iceland geochemical anomaly: origin, volcano tectonics, chemical fractionation and isotope evolution of the crust. *Journal of Geophysical Research* **90**, 10011–10026. doi:10.1029/JB090iB12p10011

Pankhurst, M. J., Morgan, D. J., Thordarson, T. & Loughlin, S. C. (2018). Magmatic crystal records in time, space, and process, causatively linked with volcanic unrest. *Earth and Planetary Science Letters* **493**, 231–241. doi:10.1016/j.epsl.2018.04.025

Passmore, E. (2009). Feeding large eruptions: crystallisation, mixing and degassing in Icelandic magma chambers. University of Edinburgh.

Peate, D. W., Breddam, K., Baker, J. A., Kurz, M. D., Barker, A. K., Prestvik, T., Grassineau, N. & Skovgaard, A. C. (2010). Compositional characteristics and spatial distribution of enriched Icelandic mantle components. *Journal of Petrology* **51**, 1447–1475. doi:10.1093/petrology/egq025

Putirka, K. D. (1999). Clinopyroxene + liquid equilibria to 100 kbar and 2450 K. *Contributions to Mineralogy and Petrology* **135**, 151–163. doi:10.1007/s004100050503

Putirka, K. D. (2008). Thermometers and barometers for volcanic systems. *Reviews in Mineralogy and Geochemistry* **69**, 61–120. doi:10.2138/rmg.2008.69.3

Rasmussen, M. B., Halldórsson, S. A., Gibson, S. A. & Guðfinnsson, G. H. (2020). Olivine chemistry reveals compositional source heterogeneities within tilted mantle plume beneath Iceland. *Earth and Planetary Science Letters* **531**, 116008.doi:10.1016/j.epsl.2019.116008

Roeder, P. L. & Emslie, R. F. (1970). Olivine-liquid equilibrium. *Contributions to Mineralogy and Petrology* **29**, 275–289.

Salters, V. J. M. & Stracke, A. (2004). Composition of the depleted mantle. *Geochemistry, Geophysics, Geosystems* **5**, Q05B07. doi:10.1029/2003GC000597

Sæmundsson, K. (1978). Fissure swarms and central volcanoes of the neovolcanic zones of Iceland. *Geological Journal Special Issue* **10**, 415–432.

Sigmarsson, O., Condomines, M. & Fourcade, S. (1992). Mantle and crustal contribution in the genesis of recent basalts from off-rift zones in Iceland: constraints from Th, Sr and O isotopes. *Earth and Planetary Science Letters* **110**, 149–162. doi:10.1016/0012-821X(92)90045-W

Sigmarsson, O., Maclennan, J. & Carpentier, M. (2008). Geochemistry of igneous rocks in Iceland: a review. *Jökull* **58**, 139–161.

Sigmarsson, O., Vlastelic, I., Andreasen, R., Bindeman, I., Devidal, J.-L., Moune, S., Keiding, J. K., Larsen, G., Höskuldsson, A. & Thordarson, T. (2011). Remobilization of silicic intrusion by mafic magmas during the 2010 Eyjafjallajökull eruption. *Solid Earth* **2**, 271–281. doi:10.5194/se-2-271-2011

Sigmundsson, F., Hreinsdóttir, S., Hooper, A., Árnadóttir, T., Pedersen, R., Roberts, M. J., Óskarsson, N., Auriac, A., Decriem, J., Einarsson, P., Geirsson, H., Hensch, M., Ófeigsson, B. G., Sturkell, E., Sveinbjörnsson, H. & Feigl, K. (2010). Intrusion triggering of the 2010 Eyjafjallajökull explosive eruption. *Nature* **468**, 426–430.doi:10.1038/nature09558

Sigurdsson, H. (1970). Structural origin and plate tectonics of the Snaefellsnes volcanic zone. *Earth and Planetary Science Letters* **10**, 129–135. doi:10.1016/0012-821X(70)90074-9

Sigurdsson, H. (2014). Þegar Bjarnarhafnarfjall var eyja. https://vulkan.blog.is/blog/vulkan/entry/1402147/.

Sobolev, A. V., Hofmann, A. W., Kuzmin, D. V., Yaxley, G. M., Arndt, N. T., Chung, S., Danyushevsky, L. V., Elliott, T., Frey, F. A., Garcia, M. O., Gurenko, A. A., Kamenetsky, V. S., Kerr, A. C., Krivolutskaya, N. A., Matvienkov, V. V., Nikogosian, I. K., Rocholl, A., Sigurdsson, I. A., Sushchevskaya, N. M. & Teklay, M. (2007). The amount of recycled crust in sources of mantle-derived melts. *Science (New York, NY)* **316**, 412–418. doi:10.1126/science.1138113

Soosalu, H. & Einarsson, P. (2004). Seismic constraints on magma chambers at Hekla and Torfajökull volcanoes, Iceland. *Bulletin of Volcanology* **66**, 276–286. doi:10.1007/s00445-003-0310-1

Sours-Page, R., Nielsen, R. L. & Batiza, R. (2002). Melt inclusions as indicators of parental magma diversity on the northern

East Pacific Rise. *Chemical Geology* **183**, 237–261. doi:10.1016/S0009-2541(01)00384-9

Sparks, R. S. J. & Cashman, V. (2017). Dynamic magma systems: implications for forecasting volcanic activity. *Elements* **13**(**1**), 35–40. doi:10.2113/gselements.13.1.35

Steinthórsson, S. (1967). Two new C-14 dates of peat samples below tephra layers of the Snæfellsjökull central volcano (in Icelandic with an English summary). *Náttúrufræðingurinn* **37**, 236–238.

Stock, M. J., Howard, K. A., Geist, D., Neave, D. A., Buisman, I., Maclennan, J., Gleeson, M. L. M. & Bernard, B. (2020). Cryptic evolved melts beneath monotonous basaltic shield volcanoes in the Galápagos Archipelago. *Nature Communications* **11**, 3767.doi:10.1038/s41467-020-17590-x

Streck, M. J. (2008). Mineral textures and zoning as evidence for open system processes. *Reviews in Mineralogy and Geochemistry* **69**, 595–622. doi:10.2138/rmg.2008.69.15

Stroncik, N. A., Klügel, A. & Hansteen, T. H. (2009). The magmatic plumbing system beneath El Hierro (Canary Islands): constraints from phenocrysts and naturally quenched basaltic glasses in submarine rocks. *Contributions to Mineralogy and Petrology* **157**, 593–607. doi:10.1007/s00410-008-0354-5

Sturkell, E., Einarsson, P., Sigmundsson, F., Geirsson, H., Ólafsson, H., Pedersen, R., de Zeeuw-van Dalfsen, E., Linde, A. T., Sacks, S. I. & Stefánsson, R. (2006). Volcano geodesy and magma dynamics in Iceland. *Journal of Volcanology and Geothermal Research* **150**, 14–34. doi:10.1016/j.jvolgeores.2005.07.010

Tait, S., Jaupart, C. & Vergniolle, S. (1989). Pressure, gas content and eruption periodicity of a shallow, crystallising magma chamber. *Earth and Planetary Science Letters* **92**, 107–123. doi:10.1016/0012-821X(89)90025-3

Tarasewicz, J., Brandsdóttir, B., White, R. S., Hensch, M. & Thorbjarnardóttir, B. (2012a). Using microearthquakes to track repeated magma intrusions beneath the Eyjafjallajökull stratovolcano, Iceland. *Journal of Geophysical Research* **117**, B00C06. doi:10.1029/2011JB008751

Tarasewicz, J., White, R. S., Woods, W., Brandsdottir, B. & Gudmundsson, M. T. (2012b). Magma mobilization by downward-propagating decompression of the Eyjafjallajökull volcanic plumbing system. *Geophysical Research Letters* **39**, L19309. doi:10.1029/2012GL053518

Thomson, A. & Maclennan, J. (2013). The distribution of olivine compositions in Icelandic basalts and picrites. *Journal of Petrology* **54**, 745–768. doi:10.1093/petrology/egs083

Thorarinsson, S. (1958). The Öræfajökull eruption of 1362. *Acta Naturalis Islandica* **11**, 6–99.

Thorarinsson, S. (1967). The eruptions of Hekla in historical times: a tephrochronological study. In: Einarsson, T., Kjartansson, G. & Thorarinsson, S. (eds) *The Eruption of Hekla 1947–1948. Societas Scientiarum Islandica*. Reykjavík, pp. 1–177.

Thordarson, T. & Höskuldsson, Á. (2008). Postglacial volcanism in Iceland. *Jökull* **58**, 197–228.

Thordarson, T. & Larsen, G. (2007). Volcanism in Iceland in historical time: volcano types, eruption styles and eruptive history. *Journal of Geodynamics* **43**, 118–152. doi:10.1016/j.jog.2006.09.005

Tryggvason, E. (1986). Multiple magma reservoirs in a rift zone volcano: ground deformation and magma transport during the September 1984 eruption of Krafla. *Journal of Volcanology and Geothermal Research* **28**, 1–44. doi:10.1016/0377-0273(86)90003-X

Ubide, T., Caulfield, J., Brandt, C., Bussweiler, Y., Mollo, S., Di Stefano, F., Nazzari, M. & Scarlato, P. (2019b). Deep magma storage revealed by multi-method elemental mapping of clinopyroxene megacrysts at Stromboli Volcano. *Frontiers in Earth Science* **7**, 239.doi:10.3389/feart.2019.00239

Ubide, T. & Kamber, B. (2018). Volcanic crystals as time capsules of eruption history. *Nature Communications* **9**, 326–326. doi:10.1038/s41467-017-02274-w

Ubide, T., McKenna, C. A., Chew, D. M. & Kamber, B. S. (2015). High-resolution LA-ICP-MS trace element mapping of igneous minerals: in search of magma histories. *Chemical Geology* **409**, 157–168. doi:10.1016/j.chemgeo.2015.05.020

Ubide, T., Mollo, S., Zhao, J. X., Nazzari, M. & Scarlato, P. (2019a). Sector-zoned clinopyroxene as a recorder of magma history, eruption triggers, and ascent rates. *Geochimica et Cosmochimica Acta* **251**, 265–283. doi:10.1016/j.gca.2019.02.021

van der Meer, Q. H. A., Bali, E., Guðfinnsson, G. H., Kahl, M. & Rasmussen, M. B. Warm and slightly reduced mantle under the off-rift Snæfellsnes Volcanic Zone, Iceland. *Journal of Petrology*, egab057. doi:10.1093/petrology/egab057.

Vink, G. E. (1984). A hotspot model for Iceland and the Vøring Plateau. *Journal of Geophysical Research: Solid Earth* **89**, **B12**, 9949–9959. https://doi.org/10.1029/JB089iB12p09949

Walter, M. J. (1998). Melting of garnet peridotite and the origin of komatiite and depleted lithosphere. *Journal of Petrology* **39**, 29–60. doi:10.1093/petroj/39.1.29

Ward, P. L. (1971). New interpretation of the geology of Iceland. *Geological Society of America Bulletin* **82**, 2991–3012. doi:10.1130/0016-7606(1971)82[2991:NIOTGO]2.0.CO;2

White, R. S., Drew, J., Martens, H. R., Key, J., Soosalu, H. & Jakobsdóttir, S. S. (2011). Dynamics of dyke intrusion in the mid-crust of Iceland Robert. *Earth and Planetary Science Letters* **304**, 300–312. doi:10.1016/j.epsl.2011.02.038

White, R. S., Edmonds, M., Maclennan, J., Greenfield, T. & Agustsdottir, T. (2019). Melt movement through the Icelandic crust. *Philosophical Transactions. Series A, Mathematical, Physical, and Engineering Sciences* **377**, 20180010.doi:10.1098/rsta.2018.0010

Winpenny, B. & Maclennan, J. (2011). A partial record of mixing of mantle melts preserved in Icelandic Phenocrysts. *Journal of Petrology* **52**, 1791–1812. doi:10.1093/petrology/egr031

Wood, B. J. & Blundy, J. D. (1997). A predictive model for rare earth element partitioning between clinopyroxene and anhydrous silicate melt. *Contributions to Mineralogy and Petrology* **129**, 166–181. doi:10.1007/s004100050330

Workman, R. K. & Hart, S. R. (2005). Major and trace element composition of the depleted MORB mantle (DMM). *Earth and Planetary Science Letters* **231**, 53–72. doi:10.1016/j.epsl.2004.12.005